

Final Report USGS/NEHRP  
Award Number 07HQGR0040

# **EARTHQUAKE HAZARD OF THE CAMARILLO FOLD BELT: AN ANALYSIS OF THE UNSTUDIED FOLD BELT IN THE SOUTHERN CALIFORNIA “HOT ZONE.”**

Duane E. DeVecchio and Edward A. Keller  
Department of Earth Science  
1006 Webb Hall  
University of California, Santa Barbara  
Santa Barbara, CA 93106-9630  
(805) 304-0036  
[duaned@umail.ucsb.edu](mailto:duaned@umail.ucsb.edu)

Lewis A. Owen and Markus Fuchs  
Department of Geology  
Geology/Physics Bldg.  
University of Cincinnati  
Cincinnati, OH 45221-0013  
(513) 556-4203  
[lewis.owen@uc.edu](mailto:lewis.owen@uc.edu)

## Abstract

The Camarillo fold Belt (CFB) in the western Transverse Ranges is composed of several active south-verging folds and reverse faults that pose an unknown hazard to nearly one million people living in the cities of Ventura, Camarillo, Thousand Oaks, and Oxnard as well as those living in the San Fernando, Simi, and Santa Clara River Valleys. Although numerous consulting reports have been generated on some of the known faults, the CFB is the only remaining fold belt between the Los Angeles fold belt and the Santa Barbara fold belt that has not been studied as a unit for the purpose of evaluating potential seismic hazard.

We integrate geologic mapping, GIS-based topographic analyses, Optically Stimulated Luminescence (OSL) and radiocarbon dating and compile previous consulting geologist reports to elucidated the relative timing of deformation on active faults, develop a chronology of deformed surfaces, better constrain the age of the Saugus Formation, and shed light on the landscape evolution in this part of the western Transverse Ranges. New mapping and age dating of the Saugus Formation exposed in the study area indicate that mapped as Saugus strata are an order of magnitude younger than previously thought (20ka vs. 200ka). This has significant implications for the timing and rates of deformation in the study area as well as the seismic hazard. Additionally it calls into question lithostratigraphic correlation of these regionally extensive strata for the purpose of assessing rates of active deformation.

Late Quaternary transpressive deformation in the CFB appears to be predominately controlled by pre-existing Miocene transtensional structures. Some of these structures are oriented parallel to the structural grain (E-W) of the western Transverse Ranges and some are north-striking. East-striking faults accommodate north south contraction with vertical uplift rates as high as 1.6 mm/yr with an interpreted maximum  $M_w = 6.4$ . North-striking transverse faults locally limit the lateral growth of faults and folds in the CFB. Transverse faults are characterized by changes in the structural style geometry and magnitude of deformation across the faults. Adjacent structural domains are typified by greater structural relief east of the transverse faults and distinct geomorphic changes characterized by greater erosional modification east of the faults. This suggests transverse faults serve as a structural barrier to deformation, but have a finite strength. Locally, late Quaternary structural domains in the CFB and within discrete fold complexes appear to young to the west and south with time.

Radiometric dating of geomorphic surfaces in this part of the western Transverse Ranges suggests the landscape evolution is strongly modulated by global climate change. A regionally extensive erosion surface was beveled on Oligocene to Pleistocene bedrock during Oxygen Isotope Stage 2 (OIS2; 18-26 ka). Preliminary investigations in the Ojai Valley to the north suggest strath cutting during this same interval (Heermance pers. comm.), which may suggest these erosion surfaces characterize a regional geomorphic marker in southern California. Downcutting following the Last Glacial Maximum (LGM; 18 ka) resulted in deep canyons cut through out the study area. Regional aggradation associated with the Pleistocene-Holocene transition resulted in accumulation of as much as 30 m of sediment that back-filled paleocanyons. Loose constraints of the aggradation event suggest deposition occurred between ~15 and 4 ka.

## Publications

DeVecchio, D.E., and Keller, E.A., 2007, Using High Resolution Topographic data to Illuminate discrete structural domains and relative rates of active tectonics, Camarillo Fold Belt: Ventura County, Southern California, Geological Society of America Annual meeting, Abstracts with Programs, vol. 39, no. 6, p. 140.

\*DeVecchio, D.E. and Keller, E.A., 2007, The role of transverse faults in accommodating lateral propagation of faults and folds: Evidence from geomorphic and structural analysis of active folding in the Camarillo Fold Belt, Ventura County, California, Eos Trans. AGU, 88(52), Fall Meet. Suppl. American Geophysical Union Annual Meeting, Abstract T33C-1476.

\*AGU Outstanding Student Presentation, Tectonophysics Session, 2007.

## INTRODUCTION

On October 1, 1987 much of the Los Angeles area was awakened by the  $M_w$ 6.0 Whittier Narrows earthquake, which occurred on a largely unrecognized thrust fault. Less than seven years later in 1994, the strongest ground motion ever instrumentally recorded in an urban area of North America was measured during the  $M_w$ 6.7 Northridge earthquake that ruptured along a completely unknown blind thrust fault and resulted in 61 deaths and ~\$20 billion in damage (Fig. 1). Consequently, many geological studies in the Los Angeles basin have concluded that thrust faults pose the greatest seismic hazard in Southern California, and accommodate most of the geodetically observed shortening across the Los Angeles area (e.g., USGS and SCEC Scientists, 1994; Dolan et al., 1995, 1997; Shaw and Suppe, 1996). Similarly, thrust faults in the Santa Barbara piedmont and Ventura County have accommodated significant shortening over the past 100 ka and are capable of generating magnitude  $M_w$ 6.5-7.5 earthquakes (e.g., Larsen et al., 1993; Gurrola and Keller, 2000; Dolan and Rockwell, 2001; Gurrola et al., *in prep.*). The presence of these fold belts within Metropolitan Los Angeles and in rapidly urbanizing areas to the north has resulted in numerous studies for the purpose of evaluating the potential seismic hazard (e.g., Blake, 1991a; Hauksson et al., 1995; Treiman 1997, 1998; Walls et al., 1998; Hitchcock et al., 1998; Oskin et al., 2000; Dolan et al., 2003). Yet, locating faults, assessing fault continuity along strike, and determining the rate and timing of deformation on active structures is often difficult because reverse faults are often blind or concealed beneath younger alluvium.

We investigate the Camarillo Fold Belt (CFB) in the western Transverse Ranges, which is composed of several active south-verging folds and reverse faults that pose a hazard to nearly one million people living in the cities of Ventura, Camarillo, Thousand Oaks, and Oxnard as well as those living in the Simi, and Santa Clara River Valleys (Fig. 2). Although numerous consulting reports have been generated on some of the known faults, the CFB is the only remaining fold belt between the Los Angeles fold belt and the Santa Barbara fold belt that has not been studied as a unit for the purpose of evaluating timing and rates of deformation. Descriptions of unlithified folded and faulted fluvial sands and silts in the CFB are omnipresent in consulting reports and paleoseismic trench logs (Blake, 1991b *and the references therein*). These deformed sediments are commonly ascribed to the Saugus Formation and assumed to have a minimum age of 200 ka. Yet, because no geochronologic investigation has been undertaken within the CFB, the true age of these strata are unknown. Our goals are to assess the relative timing and rates of tectonic folding along the active structures, better bracket the age limits of the Saugus Formation, and develop the Quaternary chronology of deformed sediments within the fold belt.

We present the Miocene to Quaternary structural development and late Quaternary geomorphic evolution of the CFB. New geologic mapping, stratigraphic analysis, and cross-sections based on subsurface water and petroleum well logs are used to illustrate Miocene deformation on several of the active Quaternary faults. To assess the late Quaternary to Holocene deformational history and relative timing of tectonic uplift of active folds we use GIS-based topographic analysis of Digital Elevation Models (DEM) and *Indices of Active Tectonics* (see Keller and Pinter, 2002) to develop a deformational chronology and to identify subsurface structures that control Quaternary deformation. In addition, we present early result from our geochronologic investigation of several of the deformed late Pleistocene to Holocene strata using Optically Stimulated Luminescence (OSL) and radiocarbon analyses. Together these data suggest the locus and lateral continuity of late Quaternary reverse faults are controlled by Miocene extensional deformation structures. Transverse faults (north-striking) locally limit the lateral propagation of folds and locally constrain deformation on the underlying faults within discrete structural domain. Locally, late Quaternary structural domains in the CFB and within discrete fold complexes appear to young to the west and south with time.

## GEOLOGIC SETTING

### Stratigraphic and Structural History

The California boarderlands west of the San Andreas fault has experienced a complex tectonic evolution following cessation of subduction during early Miocene time including: micro-plate capture, clockwise rotation of as much as 90° and syn-tectonic volcanism (e.g., Kamerling and Luyendyk, 1979; Luyendyk et al., 1980; Nicholson et al., 1994; Weigand et al., 2002; Onderdonk, 2005), as well as oblique transpressional deformation related to the “Big Bend” of the San Andreas fault (e.g., Wright, 1991; Dolan et al., 1995; Shaw and Suppe 1996; Yeats, 2004). Thick sections of volcanic and volcanoclastic rocks of the Conejo and Topanga Formations accumulated in the hangingwalls of middle Miocene transrotational normal fault-bounded basins with Oligocene Sespe Formation in their footwall (Fig. 3a)(e.g., Ehrenspeck, 1972; Willimas 1983; Ingersoll, 2001). Extensional deformation of the region continued until ca. 5 Ma, at which time development of the “Big Bend” of the San Andreas fault resulted in transpressional deformation and inversion of Miocene hangingwall basins (e.g., Crowell, 1976; Wright, 1991). The modern structure and Quaternary shortening of the CFB is strongly influenced by the Miocene extensional history as evidenced from reactivation of normal faults as west-trending high-angle reverse and north-trending tear faults throughout the region (this study, Jakes, 1980, Yeats 1988).

Following Miocene extension and volcanism, deep marine deposition in the Ventura basin (Fig. 1) ceased and the basin was filled by a westward-thickening progradational sequence of Plio-Pleistocene turbidites, shallow marine sandstone and mudstone (Pico Fm.), and terrestrial sandstone and conglomerate (Fig. 3a; Saugus Fm.). The age of the Plio-Pleistocene strata are calibrated by biostratigraphy, magnetostratigraphy, tephrochronology, and fission-track dating (*see* Yeats, 1988 *and the references therein*). Although, the age of the Pico Formation and the base of the Saugus Formation is known, the upper age limit of the late Pleistocene strata is locally unclear. Based on a single Amino Acid Racemization (AAR) age near Ventura (Lajoie et al., 1982; Yerkes et al., 1987) and age estimates from sediment accumulation rates (Blackie and Yeats, 1976), the top of the Saugus Formation is thought to be between 400-200 ka. The Saugus Formation is typically the youngest unit involved in deformation and therefore better constraints on the source, lithology, thickness, timing, and distribution of this unit are needed to assess the magnitude and rate of deformation in this part of the wTR. Undeformed sedimentary units in the Ventura basin are typically considered younger than 200 ka and given the name Quaternary older alluvium (Qoa; e.g., Kew, 1924; Jakes, 1979; Dibblee and Ehrenspeck, 1992a, 1992b).

### Regional Tectonic Framework and Physiography

The CFB lies within the western Transverse Ranges (wTR) in the hangingwall of the north thrusting Oak Ridge fault and south thrusting Malibu Coast fault (Fig. 1). Contractional deformation in southern California is the result of transpressive motion along a continental restraining bend in the San Andreas fault. Continuous GPS across the “Big Bend” of the San Andreas in southern California, suggests rates of shortening similar to that of the Himalayas, with contractional deformation between Ventura and Los Angeles being 7-10 mm/yr (Donnellan et al., 1993; Argus et al., 1999). The structural grain of this part of the wTR is characterized by east-west trending faults that accommodate left-oblique transpression, and deform Cretaceous to late Pleistocene age strata into range-scale topography (e.g., Yeats et al., 1988; Walls et al., 1998; Meigs et al., 1999; Sorlien et al., 2006). Deformation in the CFB may be kinematically linked to deformation on the more significant better studied Oak Ridge and Santa Monica fault systems (i.e., Gonzalez and Rockwell, 1991) or may represent a discrete seismic center. Although, no known earthquake surface ruptures exist within the CFB, prominent folds in late Pleistocene to Holocene sediments including those of the Oxnard Plain (delta of the Santa Clara River) attest to its activity.

The CFB is composed of several active and potentially-active east-west trending faults and folds that deform a topographic low between South Mountain to the north and the Santa Monica Mountains to the south (Fig. 2). Prominent folded strata are exposed in the Camarillo Hills north of the city of Camarillo and in the Las Posas Hills north of Santa Rosa Valley. These hills are characterized by low relief (<250 m) south-verging anticlinal folds, which are developed above north-dipping reverse faults that are locally exposed at the surface, but are commonly concealed. Anticline forelimbs on the south flanks of folds dip more steeply (~35-90°) and are more incised than the more gently-dipping backlimbs (~10-25°). The Camarillo and Las Posas Hills are separated by water gap created by Calleguas creek, which drains Arroyo Las Posas and Arroyo Simi, which flow west out of Simi Valley (Fig. 2). An additional fault trend south of the city of Camarillo and west of Calleguas Creek, herein referred to as the Camarillo anticline, uplifts fluvial strata into low relief (<25 m) undissected fold above the Oxnard Plain.

### **Previous Work in the CFB**

Regional scale mapping by Kew (1924) documented the major folds and the Simi fault in the CFB and correlated all deformed post-Oligocene marine and non-marine bedrock to the Saugus Formation. The designation Quaternary terrace deposits (Qt) was given to undeformed, but incised sediments. Utilizing subsurface petroleum data and new geologic mapping Canter (1974) and Jakes (1979) conducted detailed subsurface analysis and generated cross sections across Big Mountain and the CFB, respectively, and included them in unpublished Masters theses (Fig. 2). In both cases, post-Miocene shallow marine and terrestrial sandstone, siltstone, and conglomerate were attributed to the Saugus Formation. Their maps became the groundwork for published maps by Thomas Dibblee in the 1990's (e.g., Dibblee and Ehrenspeck 1990; 1992a, 1992b). Within the CFB, Dibblee and Ehrenspeck differentiated the marine and non-marine Saugus Formation of Jakes (1979) and Canter (1974), designating the terrestrial sediments to the Saugus Formation and gave the name Las Posas Sand to the marine sediments, which he correlated to the Pico Formation to the north. These designations imply post-Miocene sedimentation in the CFB began ~1 Ma and ended ~0.2- 0.4 Ma. Undeformed deposits were assumed to post-date deposition of deformed terrestrial strata given the name Saugus.

Within the CFB, post-Miocene strata thin from ~ 1200 m in the Oxnard plain near Camarillo (Jakes, 1990) to 900 m in the Happy Camp syncline, and pinch-out discordantly against tilted Oligocene to Miocene strata on the south flank of the Big Mountain anticline (Fig. 2 and 4). To the south in the central Las Posas Hills (Fig. 2), Pleistocene strata have a thickness <80 m and are characterized by a thin (<10 m) Las Posas Sand overlain by a terrestrial sequence of silty cobble conglomerate with interbedded soil horizons (Jakes, 1979). The entire section of Pleistocene strata thicken westward to >1500 m north of the city of Camarillo (Jakes, 1979), yet the thickness of the upper terrestrial unit at the western tip of the Camarillo Hills does not exceed a thickness of 60 m (Q4; Fig. 4)(McNamara et al., 1991; Lopez, 1991; Kile et al. 1991). Lopez (1991) also noted that the terrestrial Saugus strata unconformably overlies the lower marine member in the Camarillo Hills.

Almost nothing is known about the age of Early-Middle Pleistocene sedimentary rock in the CFB. A single AAR age in the Las Posas Hills collected from the marine Las Posas sand indicates the an approximate age of marine deposition of 450-700 ka in this part of the CFB (Boales, 1991) (Fig. 4). Although, no absolute age dates of the Pleistocene terrestrial strata overlying marine rocks (QTlp) exist in the CFB, a recent biostratigraphic age of 850-780 ka at the Moorpark Mammoth site (Wagner et al., 2007) indicates that terrestrial sedimentation north of the Las Posas Valley may have began significantly earlier than to the south in the CFB (Fig. 2).

Latest Pleistocene sedimentary units in the CFB are characterized by a thin veneer of isolated weakly dissected surficial deposits usually given the name Quaternary older alluvium (Qoa or Qoal of Jakes, 1979; Dibblee and Ehrenspeck, 1992). Older alluvial deposits are composed of gravel and silt with "B" horizons (McCoy and Sarna-Wojcicki, 1979) and are nearly indistinguishable from Saugus

strata, being differentiated by a lack of deformation and or consolidation relative to Saugus beds (Jakes, 1979). These deposits are locally conformable and unconformable with the underlying bedrock (e.g., Dibblee and Ehrenspeck, 1992). No previous age data for these deposits exist.

## METHODS OF INVESTIGATION

### Geologic Mapping

Our mapping concentrated on folded Oligocene to Pleistocene units exposed in the Las Posas and Camarillo Hills (Fig. 2). We compiled previous geologic mapping from along the south flank of South Mountain and from localities where access was limited or where new urban development obscures bedrock exposures (Kew, 1924, Jakes, 1980; Hanson, 1982, Dibblee and Ehrenspeck, 1990; Dibblee and Ehrenspeck, 1992, 1992a, 1992c; Yeats, 1988a). North of the CFB, we field checked bedding attitudes along mapped fold axes in the Saugus Formation and focused on regions where young geomorphic surfaces and sedimentary units unconformably overlie Pleistocene to Oligocene bedrock (Q3p and Q2; Fig. 4). All mapping, data collection, and sampling site locations were documented using a handheld computer running ESRI ArcPad with wireless GPS and plotted directly on orthographic photographs draped over high-resolution digital topography.

We follow previous stratigraphic nomenclature of Dibblee and Ehrenspeck (1992) of Oligocene to Middle Pleistocene strata. Specifically, we use the name Las Posas Sand (QTlp) for Pleistocene marine deposits that unconformably overlie older Oligocene-Pliocene strata. Terrestrial siltstones and conglomerates that are locally unconformable and everywhere overlie QTlp, previously mapped as Saugus Formation (e.g., Jakes, 1980; Dibblee and Ehrenspeck, 1992, 1992a), are mapped as Q(1-5) based on absolute and inferred age (Fig. 3b and Table 1).

Due to extensive agricultural use and urbanization of young geomorphic surfaces we correlated Q3p, Q2, and Q1 units (Fig. 3b) based on elevational continuity, and topographic and geomorphic expression. A greater amount of uplift and erosion of the Q3p unit and local lack of development north of the CFB on the south flank of Big Mountain enabled field investigations of several of the sedimentary deposits associated with the erosion surface. However, sedimentary deposits are thin or have been stripped, therefore we mapped the underlying strath or contact at the base of Q3p (Fig. 4).

Geologic surface relations were then compared to more than 50 subsurface well data, compiled by Jakes (1980) and Canter (1974). We relied upon previous authors lithologic interpretations of electronic logs and drill cores from well locations to 1) construct cross sections, 2) accurately locate subsurface structures, 3) determine fault and bedding dips, and 4) identify deformation on Miocene and Quaternary faults.

### GIS-based Analysis

To assess the late Quaternary to Holocene deformational history of the fold belt we used GIS-based topographic analysis of Digital Elevation Models (DEM) to quantify the stage of geomorphic development of the fold belt using *Indices of Active Tectonics* (see Keller and Pinter, 2002). We utilize two geomorphic indices to assess the relative timing of deformation and to identify subsurface structures that influence lateral growth of fault-related folds and the faults they are developed above. *Indices of Active Tectonics* include: the Hypsometric Integral ( $H_i$ ), and Catchment Denudation (Cd). We show quantification of tectonic topography and erosional denudation along youthful active structures within a finite geographic context and near homogeneous bedrock is well-suited for developing a relative deformational chronology and illuminating subsurface structural geometry of regions undergoing active shortening.

As a result of extensive residential development on active structures we found it necessary to take advantage of several different resolutions of DEM to accurately characterize the stage of geomorphic

development of the CFB. In areas of minor development, we used high-resolution 3-m Intraferometric Synthetic Aperature Radar (IfSAR) data collected in 2003 by National Oceanic and Atmospheric Administration (NOAA; <http://maps.csc.noaa.gov/TCM/>) to characterize the topography. However, where significant anthropogenic topographic modification has occurred we used lower resolution USGS 10-m National Elevation Dataset (NED; <http://seamless.usgs.gov/>), which were created from 1927 pre-development topographic maps (Fig. 5). Specifically, NED data were needed for analysis of the Santa Rosa domain and the Springville anticline and IfSAR data were used for the Simi and Camarillo Hills anticlines. We performed no GIS analysis on the Camarillo anticline because neither the pre-development aerial photos nor topographic maps show evidence of significant erosional features by which to characterize the topographic and denudational history of the fold.

We analyzed 136 catchments from the Las Posas and Camarillo Hills (Fig. 6a). Catchment size varied widely across the active structures between 0.05-1.5 km<sup>2</sup>, with no systematic relationship between the value of tectonic index and catchment area (Fig. 6b). Catchment data are divided into subsets based on structural relations to illustrate changes in the magnitude of deformation across domain boundaries. As a result of differential erosion between the more steeply-dipping forelimb and the more gently-dipping backlimb of active folds in the CFB,  $H_i$  and  $C_d$  plots focus on the forelimbs which are more deformed and have a stronger tectonic signal.

### ***Hypsometric Integral***

The Hypsometric Integral ( $H_i$ ) describe the relative distribution of elevations within the studied drainage catchment (Strahler, 1952). The hypsometric integral was calculated using the equation:

$$H_i = \frac{\text{mean elevation} - \text{minimum elevation}}{\text{maximum elevation} - \text{minimum elevation}} \quad (1)$$

The value of  $H_i$  characterize the degree of dissection and therefore can be used as an indicator of the stage of landscape development. High values of  $H_i$  indicate that mean topography within the catchment are preserved at high elevation relative to the maximum elevation, such as a recently uplifted plateau with deeply incised streams. Intermediate and low values of  $H_i$  are characteristic of a mature landscape with more dissected drainages that have established dynamic equilibrium with uplift (Keller and Pinter, 2002). Specifically, lower values of  $H_i$  are interpreted to indicate a longer period of incision and therefore older relative age.

### ***Catchment denudation***

Quantification of Catchment Denudation ( $C_d$ ) is best calculated where pre-deformational geomorphic surfaces are preserved across the structure and can be reconstructed such that an interpolated surface can be generated and the modern topography can be subtracted (Fig. 7)(Brozovic et al., 1995). Where geomorphic surfaces are rare or absent we substituted data points from the topographic crest of the folds, along drainage divides and uneroded dip-slopes where negligible surface lowering had occurred to interpolate a surface around the fold. Given the youthfulness of much of the folding in the CFB, as evidenced by unincised fold crests, we feel confident that our determinations of  $C_d$  are robust, but we consider our denudation estimates to represent minimums.  $C_d$  is calculated by:

$$C_d \text{ (m)} = \frac{\text{interpolated surface} - \text{modern topography (m}^3\text{)}}{\text{catchment area (m}^2\text{)}} \quad (2)$$

Given the limited geographic extent, as well as the nearly uniform topographic relief and bedrock involved in folds within the CFB, we assume constant erosion rate across the fold belt. Therefore, greater values of  $C_d$  can be interpreted to indicate a longer duration of erosion and thus an older inception age of tectonic uplift.

## Geochronology

We used OSL and radiocarbon geochronology to determine the age of deformed latest Pleistocene fluvial strata and to develop the Quaternary chronology and depositional history of this part of the wTR. Determination of the age of the Saugus Formation is of critical importance to consulting geologist and seismic hazard assessment in the Camarillo area because the upper age of the formation is largely unknown and it is often the youngest unit deformed by faults and folds within the CFB. However, due to the high dose rate (DR) of sediments in the CFB, sample saturation occurs more rapidly than in other localities. Therefore the maximum resolvable age by OSL in the CFB is  $\sim 45$  ka (Appendix 1). Since the top of the Saugus Formation was thought to be older than the age range of OSL dating, we focused our geochronology investigation on younger deposits (Q1-Q3) and sedimentary accumulations in the western and southern margin of the field area (Q4), where previously mapped Saugus strata was likely the youngest.

This study includes 15 OSL analyses (Fig. 4 and Table 1). OSL samples were collected from 3 paleoseismic trenches across the Camarillo anticline, deformed strata in the Springville anticline (Q4), Q3p fluvial strata preserved above strath surfaces, and from Q2 sediments on the south flank of South Mountain (Fig. 4). The OSL technique records the elapsed time since sediment was last exposed to sunlight during transport and therefore the burial age. Up to 48 aliquots (in average 24) were measured for equivalent dose ( $D_e$ ) estimation (Table 1). All samples show a high  $D_e$ -scatter with a high percentage of measured aliquots already in saturation. The high  $D_e$  scatter can be explained by insufficient bleaching of the quartz grains during the last process of sediment reworking. A precise determination of the  $D_e$  from the quartz extracts was therefore not possible. Assuming insufficient bleaching of the quartz grains during their last sediment reworking, the lower part of the dose distribution might represent the best-bleached grains. Therefore, a mean  $D_e$  was estimated from the lower part of the dose distribution. However, due to the close saturation of the samples, age estimates represent only a rough age approximation. Recovery tests indicate the reproducibility of a given dose within  $1\sigma$  error (Table 1 and Appendix 1).

A single sample of woody debris was collected for radiocarbon analyses. Sample preparation and analysis was conducted at Beta Analytic Inc. Sample age is presented in Before Present (BP) calendar years with  $2\sigma$  confidences (Table 1). We also present one additional radiocarbon age collected from a paleoseismic trench in the CFB and limited soil chronologies taken from consulting reports.

## RESULTS

### Late Pleistocene Stratigraphy

We focused our mapping and lithologic characterization on the Mid-Late Pleistocene terrestrial strata (Q1-5; Fig. 4) and their relations to the underlying Las Posas Sand and Tertiary bedrock to characterize the Late Pleistocene transpressive deformation within the CFB. A recent biostratigraphic age of  $\sim 780$  ka at the Moorpark Mammoth site (Fig. 2; Wagner et al., 2007), suggests terrestrial strata on the south flank of South Mountain are coeval with and may, in fact, be Saugus Formation sourced from the San Gabriel Mountains. This is supported by our mapping north of the CFB, which locally identifies large cobble and boulder clasts composed of granitic and metamorphic rocks consistent with a source in the San Gabriel Mountains. However in the CFB, clasts in the Q4 and Q5 units, previously mapped as Saugus Formation, are dominantly composed of pebbles consisting of Miocene Monterey Formation and Conejo volcanic clasts, with less common granitic and metamorphic clasts. Monterey shale has a source both at South Mountain and to the south in the Santa Monica mountains where the volcanic clasts are derived. Pebbles are commonly found in a red-brown silty massive matrix with no evidence of sorting or channelized flow. These deposits are intercalated with silty reddish paleosols with weak "B horizons" and carbonate cemented rhizoliths. The thickness of these sediments is not known and likely variable



across the CFB. However, where the base and apparent top are exposed, terrestrial strata are not more than 80 m in thickness. Where exposed, Q4 and Q5 strata are conformable with the underlying QTlp.

We mapped a thin veneer (<4m) of fluvial sediments that unconformably overlie a planar pediment surface beveled on Sespe and Saugus Formations on the south flank of the Big Mountain anticline and along Calleguas Creek in the CFB (Q3p; Fig. 8) (Qoa of Dibblee, 1992a, 1992b). The Q3p surface dips  $\sim 1^\circ$  to the southwest and extends from the south flank of Big Mountain, north of the city of Moorpark, westward to the approximate location of the town of Somis, where it dips below the west Las Posas Valley (Fig. 2 and 4). Sediments associated with the Q3p pediment surface are dominantly flat lying and characterized by intercalated well-sorted coarse-grained cross-bedded sand and cobble conglomerate with clasts composed of compositionally identical rocks to those found in the Sespe and Saugus Formations. Coeval sediments exposed in the Camarillo anticline (Fig. 3; Q3a) are compositionally and texturally similar and likely represent a distal facies of the Q3p sediments.

Latest Pleistocene gravels (Q2) are preserved east of the Wright Road fault, comprise the broad surface of the west Las Posas Valley, and fill topographic lows along the south flank of South Mountain (Fig. 4). The Q2 unit is composed of massive greenish silt beds that contain fragments of Monterey shale. Catchments along the south flank of South Mountain are characterized by broad flat-floored valleys that locally contain as much as 30 m of Q2 fill currently being incised by modern drainages (Fig. 9). The true thickness of this unit is not known and may vary along strike.

## Geochronology

### *Camarillo Anticline*

Paleoseismic trenches across the crest and forelimb of the Camarillo anticline were excavated for the purpose of determining the magnitude of deformation along the Camarillo fault (Fig. 2). Trenches were logged by the managing consulting companies and field checked during sampling to determine the depositional environment and stratigraphic context of OSL sample sites. The western Earth Systems trench site consists of 2 excavations at the western-most exposure of the anticline, from which we collected 3 OSL samples from Q3a strata (Fig. 10a and b). Evidence of minor hangingwall deformation was observed in the trenches, but the Camarillo fault was not encountered. Two samples were collected within 3 m of each other from the southern-most tilted fluvial strata in trench B. Q3a strata strike N88W and dip  $36^\circ$ SE. Samples 01 and 02 are within error and give an age range from  $\sim 23$ -21 ka (Table 1). Sample 03 was collected from flat-lying Q3a silty-mud on the crest of the anticline and gave an older age of  $32.27 \pm 6.29$  ka, suggesting the crest of the anticline experienced erosional beveling during early uplift exposing lower stratigraphic units (Fig. 10b).

The eastern trench, located  $\sim 100$  m east of the Earth Systems trench site, was excavated by GeoSoils Inc. and consisted of a single trench, 100m long and 15m deep (Fig 10c). Similarly, the eastern GeoSoils trench did not encounter the Camarillo fault. The trench extends from flat-lying Q3a strata at the crest of the Camarillo anticline, across the south-dipping forelimb and back into flat-lying strata south of the fold in the Oxnard plain. Evidence for erosional beveling on the crest of the anticline during uplift was also identified in the the GeoSoils trench, which showed truncated south-dipping forelimb strata near the crest of the fold (Fig. 10c). Four samples were collected and dated from the trench, all of which underlie a soil developed on the forelimb with an age estimate of  $\sim 30$  ka (Shlemon, personal comm.). Sample 04 came from a fluvial Q3a sand that strikes N80W and  $36^\circ$  south and gives an age of  $27.29 \pm 2.90$  (Table 1). Sample 05 and 06 are within error and give an age range of  $\sim 27$ -32.5 ka (Table 1 and Fig. 10c). These samples are from an upper silty-mud unit, interpreted to be a colluvial wedge deposit that developed as a result of tectonic uplift along the Camarillo anticline. Sample 07 comes from an upper colluvial deposit that underlies the former and gave an age of  $40.76 \pm 3.81$  ka.

Samples 01-02 and 04-06 from the forelimb of the Camarillo anticline are all internally consistent and in agreement with the soil chronology, indicating an age <30 ka for south-tilted Q3a strata in the

forelimb of the Camarillo anticline. We believe the older age given by sample 07, which is in disagreement with all other OSL dates and the soil chronology, is likely the result of insufficient bleaching and inheritance from lower stratigraphic units being exposed along the eroding anticlinal crest during uplift. Sample 08 gave an age of  $18.26 \pm 1.76$  ka and comes from a flat-lying silty mud unit of the Oxnard plain that overlies fluvial sand at the southern extent of the trench (Fig 10c). This sample is likely not involved in the deformation.

### ***Springville Anticline***

Samples 09 and 10 were collected from a recently excavated agricultural cut through the western-most tip of the west-plunging Springville anticline (Fig. 4). Sample 09 gives an age of  $34.39 \pm 9.96$  ka and comes from a trough cross-bedded fluvial sand (Q4) that strikes N45W and dip  $12^\circ$  SW (Table 1). Sample 10 comes from a massive silty bed that underlies the cross-bedded sand. All analyzed aliquots of this sample were close to saturation and only a minimum age of 46.17 ka could be calculated. Saturation of sample 10 either suggests that the deposition of the silty bed occurred  $>46$  ka or the old age is the result of insufficient bleaching during sediment reworking (Appendix 1).

### ***Quaternary Pediment (Q3p)***

Three samples were collected for OSL analysis from the sediment overlying the Q3p erosion surface (Fig. 8). Samples 12 and 15 are separated by  $\sim 15$  km (Fig. 4) and gave consistent ages of  $26.92 \pm 4.06$  ka and  $24.69 \pm 1.98$  ka, respectively (Table 1). Sample 18 is slightly younger and gives an age of  $19.24 \pm 1.88$  ka (Fig. 8). An additional age on the Q3p surface comes from a paleoseismic trench, north of the Santa Rosa Valley fault, which exposed south-dipping Qp gravel that have gave a radiocarbon age of  $23.28 \pm 1.04$  ka (*see* Blake, 1991a; Treiman, 1998 *and the references therein*). Together the OSL and radiocarbon ages suggest the sedimentary deposits associated with the Q3p surface were deposited sometime between  $\sim 17$ -30 ka.

### ***Latest Pleistocene alluvium (Q2)***

Two OSL analyses were performed on samples collected from the Q2 unit. Both sample 17 and 19 come from back-filled valleys along the south flank of South Mountain (Fig. 8). Sample sites are separated by  $\sim 8$  km and are both within 3 m of the geomorphic top of the Qoa unit at each locality (Fig. 3). The eastern most sample (17OSL07) gave an age of  $12.60 \pm 1.38$ . Sample 19 gave an age of  $4.78 \pm 0.47$  (Table 1).

## **Structural Domains and Transverse Faults**

We have divided the CFB into four discrete structural domains defined by fault segment boundaries and differences in the relative timing and style of deformation; the Simi fault zone, Santa Rosa fault zone, the Springville fault zone and the Camarillo fault zone (Fig. 11). Fault segment boundaries are commonly occupied by transverse faults that juxtapose lower stratigraphic units on the east against higher stratigraphic units on the west (Fig. 11; A-A').

### ***Simi Domain***

The easternmost zone of faulting within the CFB contains the western extent of the well-studied Simi fault. East of the CFB, the Simi fault delineates the northern extent of Simi Valley and the southern boundary of the Santa Susana Mountains and has been shown to have Quaternary slip (Hitchcock et al., 2001; Treiman, 1998). Within the CFB, the Simi fault zone is composed of several potentially active splays including two northern segments and a southern concealed splay (Fig. 11). The northern splays are exposed in the core of the east-trending Las Posas anticlinal ridge that is defined by a thin veneer ( $<20$ m) of east-striking oppositely dipping Q5 strata (Fig. 11). Previous mapping of the northern Simi fault either show the fault as a continuous structure or as a pair of right-stepping en echelon faults (Dibblee and Ehrenspeck 1990; Jakes, 1980, respectively) that dip steeply ( $75$ - $85^\circ$ ) to the north. Although the fault is poorly exposed in parts of the Las Posas hills, our geologic and geomorphic

mapping of the Las Posas Hills suggests the fault is not continuous, as such we depict the fault as a right-stepping pair of faults (Fig. 11).

All of the faults within the Simi domain show evidence of Miocene deformation. The northern Simi fault splays have opposite sense of Miocene normal displacement. North of the northeastern Simi fault the Saugus Fm. rests unconformably on north-dipping Oligocene Sespe Fm. (Tsp), though south of the fault, Q5 strata lie on Miocene strata of Topanga Fm. or Conejo volcanic rocks (Fig. 11). In contrast, north of the northwestern Simi fault Q5 rests on a thick (180 m) section of Miocene volcanic rocks and on Sespe Formation to the south (Fig. 11). Miocene normal displacement on the Simi fault splays is consistent with previous mapping of the fault in north Simi Valley (Hanson, 1982, Dibblee and Ehrenspeck, 1992b). A cross section through the northern Simi fault splays, based on subsurface data and our mapping, indicates 35-40 m of Quaternary north-side-up slip on the northern fault segments (Fig. 12). We suggest the northern Simi faults are involved in the folding and locally accommodate a fraction of the contractional strain within the Las Posas anticline. However, the majority of Quaternary deformation of the Las Posas anticline is the result of displacement on the southern splay of the Simi fault (Fig. 11; Santa Rosa fault of Treiman, 1998).

Similar to the northern strands, there is strong evidence of Miocene down-to-the-south displacement on the southern strand of the Simi fault. Subsurface wells on either side of the southern Simi fault show the top of the Sespe Formation is displaced 1.5 km down in the south and overlain by a thick section of Topanga Fm. and Conejo volcanics (Fig. 11). The Simi fault also uplifts the base of the Saugus Formation on the north side by ~111 m (Fig 12). Although the southern splay of the Simi fault is largely concealed along the range front, a recent paleoseismic trench in foreland latest Pleistocene alluvial fan sediments that show evidence of faulting (Gurolla, personal comm., 2007).

The southern splay of the Simi fault offsets the north-striking East Baranca fault in the eastern Las Posas Hills. The East Baranca fault juxtaposes Q5 strata on the west against folded Sespe and Topanga Fms. to the east and truncates the northern Simi fault (Fig. 11). These relations suggests activity on the southern splay of the Simi fault west of the East Baranca fault postdates the deposition of the base of Q5, while east of the fault uplift and folding were likely being accommodated on the Simi fault and Simi anticline (Fig. 2). There is no evidence that the East Baranca fault deforms the Q3p surface in the northern Las Posas Hills (Fig. 11). Therefore, the southern Simi fault in the CFB likely became active following deposition of the base of the Saugus at this location and before approximately 23 ka. We suggest the southern splay of the Simi fault in the CFB is the westward extension of the active Simi fault studied by Hitchcock et al. (1998).

All splays of the Simi fault and the east-trending Las Posas anticline terminate to the west at a previously unmapped NNW-striking cross fault, herein referred to as the Camarosa fault (Fig. 11). Similar to the Simi fault splays, the Camarosa fault appears to have an older Miocene and younger Quaternary deformational history. The fault is manifested by 1) the termination of all fault and folds to the east and west of the fault, 2) sedimentological and thickness change in the Saugus and Topanga Fms., 3) subsurface juxtaposition of the Sespe Fm to the east against Topanga and Q5 to the west, 4) juxtaposition of the Q3p surface and the Q5 strata, 5) changes in latest Pleistocene vertical uplift rates across the fault, and 5) distinct changes in the relative timing and geomorphic expression of faulting and folding (discussed later in GIS-based analysis).

East of the Camarosa fault, the top of the Sespe Fm is overlain by a thin (~40 m) veneer of Topanga strata capped by Saugus Fm. and exposed at an elevation of 152 m. Yet, west of the Camarosa fault, subsurface well data show the top of the Sespe Fm. at a depth of 450 m and overlain by ~600 m of Topanga strata (Fig 11), which suggests ~140 m of down-to-the-west Miocene displacement across this structure. Post mid-Pleistocene transpressional deformation is characterized by 91 m of uplift of the base Q5 (east-side-up) (Fig. 11). In addition, separation of the Qp surface and the long profile of Calleguas

Creek increases by 13 m to the west of the Camarosa fault, indicating post 23-26 ka differential uplift or down-cutting west of the Camarosa fault (Fig. 13).

### ***Santa Rosa Domain***

The Santa Rosa structural domain is bound on its eastern margin by the Camarosa fault and on the west by the NNW-striking Somis fault. The domain is characterized by the largely undissected uplifted Q3p surface to the south and anticlinal folds in Q5 to the north beneath the Upland Rd. ridge (Fig. 11). Four WSW-trending fault strands deform the domain. From north to south they include: the northern Santa Rosa fault, the central Santa Rosa fault, the southern Santa Rosa fault, and the Santa Rosa Valley fault (Fig. 11). Although the Santa Rosa domain is densely urbanized and much of the traces of these faults are concealed, the location of the faults and sense of displacement is known or can be inferred based on numerous paleoseismic trenches, subsurface well data and geomorphic expression. Previous paleoseismic trench logs show the northern and central Santa Rosa faults steeply dipping with as much as 25 m of south-side up displacement of “younger alluvium” (probably Q5) (Tierra Tech, 1978; Buena Engineers, 1987; Boales, 1991). The northern and central splays are likely back-thrusts of the north-dipping southern splay of the Santa Rosa fault and may accommodate a component of left-lateral deformation (Fig. 14).

The southern Santa Rosa fault, juxtaposes Las Posas Sand and Q5 in the hangingwall against Q3p to the south (Fig. 11 & 14). Treiman (1998) interpreted an 18-27 m zone of brecciation and 5-8 times thickening of soil in a paleoseismic trench across the southern Santa Rosa fault as strong evidence for young displacement on the southern strand of the Santa Rosa fault. Cross-sections across the Santa Rosa domain suggest hangingwall thinning and ~75 m of up-to-the-north displacement of the base of Q5 (Fig. 14).

South of the Santa Rosa faults, uplift and folding of the Q3p surface is the result of north-side-up displacement on the Santa Rosa Valley fault, which terminates to the east of the Camarosa fault (Fig 11 & 14). Uplift of the Q3p surface along the Santa Rosa Valley fault has produced a 35 m scarp and open anticline (Santa Rosa Valley anticline) in the hangingwall of the fault. The uplifted Qp surface in the hangingwall is nearly undissected to the west, becoming more dissected eastward.

The Somis cross fault defines the western margin of the Santa Rosa Domain and is completely concealed beneath Holocene alluvium of Calleguas Creek and likely controls the position of the water gap between the Las Posas and Camarillo Hills. The fault was first mapped by Bailey (1951) and shown as a Miocene down-to-the-west normal fault. Jakes (1979), used subsurface petroleum well data to argue for post-Miocene left-lateral offset on the Somis fault. Nowhere is the Somis fault exposed at the surface and determination of the pre-Quaternary sense of offset of this fault is beyond the scope of this paper. However, based on subsurface well data it is apparent that significant tilting east of the Somis fault occurred post-middle Miocene, where west of the fault, Plio-Pleistocene strata everywhere are conformable with the underlying Miocene strata. This may suggest the Somis fault served as a tectonic boundary to late Miocene extensional deformation, separating discrete structural domains. Evidence of Plio-Pleistocene activity on the Somis fault is best illustrated in a USGS water resources cross section based on water wells (Hanson et al., 2003). The cross-section shows uplift and erosion of the Upper Hueneme aquifer (Pico/Las Posas Fms.) east of the Somis fault beneath west Las Posas Valley, indicating Quaternary uplift east of the fault.

### ***Springville Domain***

West of the Somis fault and north of the city of Camarillo, the Camarillo Hills expose deformed Las Posas Sand and Q5 strata folded along the Springville fault zone (Fig. 11). The Springville fault zone extends westward from Calleguas Creek for ~9 km where it abruptly terminates in the Oxnard plain and the inferred Wright Road fault (Fig. 11). Most of the faulting occurs along the south side of the hills and is concealed beneath younger alluvium. Deformation in the Camarillo Hills results in two discrete doubly-plunging asymmetric south verging-anticlines within the Camarillo Hills: the Springville and

Camarillo Hills anticlines (Fig. 11). Dibblee and Ehrenspeck (1992a) depict the Springville fault zone as a continuous curvilinear north-dipping fault. Based on our geomorphic mapping, interpretation of pre-development air photography, and the presence of a pair of en echelon anticlines we suggest the Springville fault zone is composed of a pair of north-dipping left-stepping reverse faults; herein referred to as the southern and northern Springville faults (Fig. 11 and 15). This interpretation is consistent with Jakes (1979) who previously proposed a southern Springville fault concealed below the Quaternary alluvium based on subsurface offset in petroleum cores of the upper Sespe Formation unconformity. The accommodation zone between the two faults and their folds is characterized by an ENE-trending topographic low and west flowing drainage off the nose of the Camarillo Hills anticline. Due to extensive urbanization of the area, new investigations within the accommodation zone are not possible. However, it should be noted that Leighton and Associates (1991) documented abundant evidence of steep NE- and NW-trending tear faults with large lateral offsets in the area of the accommodation zone. Additionally, paleoseismic trenching along the southern margin of the Camarillo Hills in the same area identified a sub-vertical N15E trending fault whose inferred trace corresponds to the termination of both folds in the Camarillo Hills (Glenn, 1991). Therefore, we consider it possible that the accommodation zone between the northern and southern strands of the Springville fault may be characterized by a north-trending fault similar to other transverse fault observed in the CFB (Fig. 11).

As a result of urbanization of the Springville anticline, numerous consulting reports and geologic investigations have been completed on the southern Springville fault (*see* Blake et al., 1991b). However, the dip of the fault and magnitude of slip of the southern Springville fault are still debated. Jakes (1979) argues strongly for a steeply north-dipping fault (75-85°) based on subsurface data, in contrast with paleoseismic trench data that indicate surface fault dips of 15-45° (e.g., Kile et al., 1991; Ruff and Shlemon, 1991; Gonzalez and Rockwell, 1991). Based on previous work and our surface mapping of the fault trace, we believe the southern Springville fault dips ~70° to the north and flattens to more shallow dips within a few 100's of feet of the surface, which may be common in inverted extensional basins (McClay and Buchanan, 1992). Subsurface displacement estimates of the top of the Sespe Formation by Jakes (1980) suggest 275m of north-side up displacement yet the maximum displacement observed from paleoseismic trenching is only 10 m (Whitney and Gath, 1991). Given the total topographic relief of the Springville anticline is only ~80 m, subsurface estimates suggest a significant volume of Q4 strata should have been tectonically uplift and eroded away, which is inconsistent with the preservation of the forelimb of the fold and lack of erosion observed across this structure. Offset of the top of the Sespe Formation is likely the result of Miocene down-to-the south displacement, which is consistent with 3-fold increase in the thickness of the Conejo volcanics and Topanga Fms. to the south (Fig. 15). Reactivation of the Miocene structure as a steeply- north-dipping reverse fault accommodates ~ 75 m of vertical motion since the deposition of the base of Q3.

Significantly less paleoseismic data exist for the northern Springville fault and most of what can be derived comes from geologic mapping and subsurface well data. The fault zone along the south limb of the Camarillo Hills anticline is characterized by faceted spurs, steep to locally overturned Saugus strata on the southern forelimb, and deeply-incised drainages. Headward erosion of south flowing drainages have driven the drainage divide north of anticlinal axis and expose lower Las Posas Sand strata (Fig. 11). The steeper dips and absence of terrestrial Q(3-4) strata on the forelimb of the Camarillo hills anticline suggest a greater magnitude of folding and slip on this segment of the Springville fault zone. Based on a test pit across the northern strand, Bailey (1951) showed the fault dipping 25° to the north. Alternatively, the fault may dip steeply similar to other structures in the study area, so we propose two possible fault plane geometries (i.e., 25° and 75°; Fig. 15). The vertical offset on the northern Springville fault must exceed the total vertical relief (145 m), however, the magnitude of displacement on the fault is highly dependant on the two different fault geometries, which we will discuss latter.

The inferred Wright Rd. fault is characterized by a prominent 20 m-high topographic scarp that separates the Oxnard plain on the west and the latest Pleistocene surface (Q2) of the west Las Posas Valley to the east (Fig. 11). This location also corresponds to the abrupt westward termination of the Springville anticline and the location where shortening on the Oak Ridge fault goes to zero (Yeats and Huftile, 1995, Yeats 1988) and the Oak Ridge fault becomes more north-striking and is characterized by strike-slip displacement (Nicholson personal comm., 2008). The Wright Rd. fault has been hypothesized to exist by numerous consulting geologists and recommended for earthquake zoning by the California Geological Survey (Treiman, 1997). Pre-agricultural development photos show tonal lineaments suggestive of a low en echelon scarp in young sediments of the Oxnard plain that extends southward from the Q1 surface toward the western tip of the Springville anticline. Although extensive cultivation of the region has modified the feature, a 2 m-high scarp can still be traced across the landscape most notably crossing Wright road near Beardsley Creek (Treiman personal comm., 2007). We interpret these geologic and geomorphic evidence to suggest the Wright Rd. fault is responsible for the scarps in the Oxnard plain west of the west Las Posas Valley and likely limits the westward lateral growth of the Springville fault zone. Thus the Wright Rd. fault may be related to deformation on the Oak Ridge fault. Radiocarbon dating of Oxnard plain sediments adjacent the 2m-high scarp suggests slip on the Wright Rd. fault occurred within the last 1,000 years (Table 1).

#### ***Camarillo Domain***

The Camarillo fault, which underlies the city of Camarillo is manifested by the 3 km-long, 24 m-high east-trending anticline that plunges to the west beneath the Oxnard Plain. The fold terminates abruptly to the east and has likely been modified by Calleguas Creek (Fig. 2). The anticline is completely undissected in pre-development aerial photographs. Several recent paleoseismic trenches along the Camarillo fault indicate forelimb bedding plains dip as much as 40° south (Fig. 10). One large deep trench extended for ~100 m from the gently north-dipping backlimb across the anticlinal axis and south-dipping forelimb and encountered flat strata in the foreland 15 m below the top of the trench. However, the fault was not encountered, indicating the fault has not yet propagated to the surface and is blind at this location.

#### **GIS-Based Analyses**

##### ***Hypsometric Integral ( $H_i$ )***

***Simi and Santa Rosa Domains:*** We considered 33 catchments along the south flank of the Las Posas hills that ranged in size from 0.6- 1.5 km<sup>2</sup>; twenty-five from the Simi domain and 8 from the Santa Rosa domain (Fig. 16a). Calculated values of  $H_i$  ranged between 0.36 - 0.86, where higher values of  $H_i$  are indicative of more youthful terrains (Keller and Pinter, 2002). Standard deviation ranges from 0.07 within the Simi domain, to 0.13 within the Santa Rosa domain. Within the Simi domain 88% of the catchments have values less than 0.55, while 75 % of the catchments in the Santa Rosa domain have values greater than 0.64 with 37.5 % of the catchments being 0.80 or greater. Statistical means of  $H_i$  for the Simi and Santa Rosa domains are 0.45 and 0.69, respectively (Fig. 16a). Statistical analysis of these data indicate sample datasets are significantly different at 95% confidence.

***Camarillo Hills and Springville Domains:*** We considered 25 catchments from 3 structural zones along the south flank of the topographic uplift along the Springville fault zone that ranged in size from 0.5-1.3 km<sup>2</sup>; thirteen basins along the Camarillo hills anticline, 8 along the Springville anticline, and 4 within the accommodation zone between the two folds (Fig. 16b). Calculated  $H_i$  values range from 0.37- 0.68 suggesting the presence of mature to semi-youthful topography, respectively (Keller and Pinter, 2002). Standard deviation of the sample populations is 0.08 with the greatest value being within the accommodation zone at 0.10 and decreasing east and west to 0.05 and 0.06, respectively. For the Camarillo Hills anticline, 100% of the catchments have  $H_i$  values less than 0.57, with a statistical mean 0.48. Catchment along the Springville anticline to the west have a statistical mean of 0.58 with all

catchments having values greater than 0.57 (Fig. 16b). Statistical analysis of data from the Springville and Camarillo anticlines indicate sample means are significantly different at 95% confidence. Although, data from the accommodation zone are significantly different at the 95% confidence interval from data from the Camarillo hills anticline, there is no statistical difference between the Springville anticline and catchments within the accommodation zone.

### **Catchment Denudation ( $C_d$ )**

**Simi and Santa Rosa Domains:** Catchment denudation was calculated for the same 33 basins utilized in the  $H_i$  index from the Las Posas hills, and differentiated across 3 structural zones; 16 catchments from along the eastern and 9 from along the western segments of the northern the Simi fault, and 8 from the Santa Rosa domain. Calculated values of  $C_d$  range from 0.5 – 35.6 m with a mean of 12.1 m (Fig. 17a). There is no statistical difference between either of the two northern segment of the Simi fault. Mean  $C_d$  values for the northern Simi fault are 14.46 m and 15.2 m. Catchments from the Santa Rosa domain have a mean  $C_d$  value of 3.4 m with 75% of the catchments below 1.9 m. Data from the Simi domain are statistically significant from those in the Santa Rosa domain, with the whole dataset showing a five fold decrease in erosion across the Camarosa fault.

**Camarillo Hills and Springville Domains:** The same catchments used in the  $H_i$  index were utilized to calculate  $C_d$  values from the Camarillo hills.  $C_d$  values ranged from 1- 31m with a mean of 8.1m (Fig. 17b). Mean erosion decreases from east to west along the Camarillo hills from 12.0 along the south limb, to 3.9 m within the accommodation zone, to 2.8 m along the Springville anticline. No significant difference can be shown between mean erosion within the accommodation zone and the Springville anticline. However, there is a ~3-fold decrease in catchment denudation from the Camarillo Hills anticline to the Springville anticline to the west.

### **Earthquake Hazard**

We identify ten fault segments within the CFB that are Active (A), Apparently Active (AA), or Potentially Active (PA) (Table 2). Fault segment lengths are estimated based on geometric, geomorphic, and structural discontinuities that indicate lateral fault termination at segment boundaries. Most fault segments are relatively short as a result of transverse faults with the exception of the southern Simi fault which extends for ~ 18 km to the east of the CFB for a total length of 24 km (Table 2). Estimates of moment magnitude based on fault rupture area and fault length were determined from regression relationships defined Wells and Coppersmith (1994).

For moment magnitude calculations, based on fault area, we assumed a rupture depth of 12 km for faults that dipped steeply (~75°). We assume shallow dipping structures like the Northern Springville fault “solution A” (Fig.15) to be non-seismogenic or coseismic with the Oak Ridge fault, which it likely joins at depth. Similarly, we believe that the transverse faults are not likely discrete seismic sources but slip coseismically with adjacent contractional faults.

Potential moment magnitudes from the CFB are estimated to be within the range  $M_w$  5.2 to  $M_w$  6.4, with the southern Simi fault characterizing the largest hazard for the region (Table 2). A maximum moment magnitude of  $M_w$  6.7 for the southern Simi might be expected if the fault was able to rupture through the intervening transverse faults and link with the Santa Rosa and Springville fault zones.

## **DISCUSSION**

### **Fault Segment Boundaries and Transverse Faults**

Fault segment boundaries within the CFB are characterized by transverse faults. Transverse faults appear to have controlled the lateral growth of late Quaternary contractional faults and folds in the CFB. Where more than one structural domain forms a single topographic feature (i.e., Camarillo Hills and Las

Posas Hills), anticlinal folds plunge on either side of the transverse faults. This suggests the faults serve as a barrier to lateral propagation of folds and the underlying faults. Available data does not indicate whether faults within discrete structure domains grew by fault tip migration or whether fault tips have remained fixed at the segment boundaries through time. However, given that many of the active reverse faults are inherited structures, we suggest fault lengths are likely fixed through time and folds grew strictly by amplification rather than lateral propagation. Yet, discrete structural domains and the fold belt as a whole appears to young to the west.

Changes in structural relief across segment boundaries indicate either a differences in the rate of uplift or changes in the timing of deformation. In all cases, structural relief (Fig. 11; A-A') and erosional denudation in adjacent structural domains are greater east of a given transverse fault (Fig. 17). In contrast, hypsometry decreases east of the faults (Fig. 16). These geologic and geomorphic data together with estimates of fault slip rates (Table 2) support the interpretation that folds are younging to the west and are not the result of westward decrease in slip rate. In fact, differential uplift of the Qp3 surface across the Camarosa fault indicates local increases in latest Pleistocene rates of deformation to the west (Fig. 13). Where slip rates are well known based on vertical uplift of well-dated deposits, the rates of deformation fall in a narrow range between 1 mm to 1.5 mm/yr across the fold belt (Table 2). Abrupt changes in topography and structural relief across segment boundaries suggest folds east of a given transverse fault amplify for a period, before strain gradients at the fault- and fold-tip increase to a critical point, at which time the transverse fault is breached and faults and folds are able to propagate into the adjoining structural domain to the west (i.e., East Baranca fault). Alternatively, deformation in the adjacent domain may be accommodated on a new suite of structures without cutting the transverse fault (i.e., Camarosa fault). In the later case, we would expect changes in the loci of deformation as well as change in the geometry and orientation of active structures.

Deformation associated with the Camarosa fault, which bounds the eastern terminus of the Santa Rosa Domain perhaps best illustrates the complex poly-genetic character of transverse faults in the CFB and their role in limiting the lateral growth of fold and faults in the study area. Approximately 600 m of offset of the top of the Sespe Formation across the fault can be attributed to down-to-the west Miocene transtensional deformation (Fig. 11). Later transpressional deformation across the fault is characterized by 94 m of up-to-the-east deformation of the base of Pleistocene strata, as a result of folding and slip on the southern Simi fault. The large and abrupt changes in dissection across the Camarosa fault (Fig. 16a and 17a) and increase in structural relief to the east (Fig. 11; A-A') suggest post-Pleistocene uplift and amplification of the Las Posas anticline, east of the Camarosa fault, occurred while deformation west of the fault was likely absent. We do not know when deformation propagated westward into the Santa Rosa Domain. Nevertheless distinct changes in the geometry of faulting and folding occur across the domain boundary suggesting the two domains remain discrete. This is supported by ~10 m of differential uplift of the Q3p surface across the Camarosa fault, which indicates a greater rate of post ~23 ka deformation in the Santa Rosa Domain (Fig. 13). Given the close spatial relationship between the eastern tip of the central Santa Rosa fault and the western extent of the southern Simi fault, the Camarosa fault may have been breached at this location, although locally the Camarosa fault still appears to impede lateral growth of several of the active faults and folds within the two domains.

Cross section A-A' (Fig. 11) illustrates that transverse faults all have a component of dip-slip motion. However, we believe these faults are dominantly strike-slip faults that accommodating differential shortening and vertical uplift along the strike of the CFB. Oblique-slip displacement on transverse faults is likely the result of reverse displacement on adjacent east west striking faults. Therefore, the magnitude and rates of deformation on transverse faults are similar to the adjacent contractional faults and seismic slip is likely coseismic with slip on the reverse faults (Table 2).



## **Sedimentation History**

This research provides new insight into the erosional and depositional processes that shaped the landscape in this region of the wTR. These processes are modulated by late Pleistocene to Holocene climate change and local tectonics. Our investigation indicates deposition of fluvial sands and conglomerates throughout the CFB, some of which were previously mapped as Saugus Fm., overlap in age with previously mapped younger alluvium (Qoa/Qoal Dibblee and Ehrenspeck, 1992& 1992a) (Fig. 18). Because we believed the upper age limit of much of these strata were beyond the temporal range of OSL, we did not extensively sample previously mapped Saugus strata and thus the full depositional age range of oldest terrestrial deposits in the CFB (Q5) is still unknown. However, we use calculated slip rates 1.0 mm/yr to 1.5 mm/yr from with the CFB to infer the age of Q5 along strike. If slip rates are in fact consistent along strike of the fold belt as our data suggest, depositional base of Q5 may be as old as 160 ka in the Las Posas hills (Table 2).

The composition, source, thickness, character, and timing of deposition of terrestrial strata in the CFB are distinctly different from Saugus strata described to the north and east. The composition of clasts in alluvial deposits indicates sediments were derived from South Mountain and the Santa Monica Mountains and not from uplift of the San Gabriel Mountains (Saugus source terrain). Minor granitic and plutonic clasts in Q5 strata are likely recycled from eroding Saugus strata on the south flank of South Mountain, which was uplifted sometime after 200-400 ka (Blackie and Yeats, 1976; Yeats, 1988).

Uplift of South Mountain would have resulted in regional uplift of the Camarillo area within the hangingwall of the Oak Ridge fault and isolation of the Camarillo area from the ancestral Santa Clara river that delivered sediment for the Saugus Formation deposited at South Mountain. Folding along the axis of South Mountain exposed the Saugus and the underlying Monterey shale, which provided a sediment source for alluvial fans (Q5) that filled the shallow marine basin to the south (CFB; Fig. 19c). Deposition in the uplifting hangingwall basin resulted in deposition of a thin section (<100 m) of terrestrial alluvial deposits as sediment bypassed the basin and were transported to the location of the Oxnard plain to the west. This is in sharp contrast to the thick (1-3 km) sequence of fluvial Saugus conglomerate and sandstones that accumulated in the subsiding Middle Pleistocene basin to the north. Deposition of terrestrial strata, derived from the Oak Ridge fault uplift and the Santa Monica Mountains, continues until the present in the Oxnard plain and along Calleguas Creek, except where local deformation has uplifted and folded these rocks along active structures in the CFB. The age of the base of terrestrial deposition youngs to the west as local base level fell and the marine environment regressed westward. OSL dates from Q4 at the western tip of the Springville anticline which overlie marine sediments indicate that locally the base of the terrestrial strata is as young as ~45 ka in the western region of the CFB.

### ***Quaternary Pediment (Q3p)***

Sediments overlying the Q3p erosion surface were dated using both OSL and radiocarbon analyses at four different localities, three of which gave consistent ages (22.7- 24.3 ka), while the fourth gave a younger age (19.24±1.88). If we assume the age of the sediments locally reflect the age of bedrock planation (Mackin, 1937; Bull, 1990), and creation of large erosion surfaces likely takes 10<sup>3</sup> yrs (Hancock and Anderson, 2002), the age of the sediments should be represent a time interval corresponding to the minimum length of time that the surface was active. We suggest lateral bedrock planation associated with the Q3p surface occurred during the interval from 26-18 ka based on available data and associated analytical errors (Fig. 18). This time period falls within Oxygen Isotope Stage 2 (OIS2) and overlaps a period of sustained sea level low during the Last Glacial Maximum (LGM)(see review in Mix et al., 2001). Given the strong temporal correlation of the data to the LGM, we feel confident the genesis of the Q3p surface is climate-related rather than tectonic. However, the preservation of the surface is certainly the result of post-LGM uplift. The landscapes response to climate change (aggradation vs. degradation) is still debated (e.g., Pazzaglia et al., 1998; Hancock and

Anderson, 2002) and the climate conditions of the study area during the LGM (dry vs. wet) are not well known. Of particular interest to understanding the development of the Q3p surface is how the climate changed during the transition from interstadial (OIS3) to the LGM (OIS2). Pluvial lake studies from Death Valley and the Mojave Desert indicate that lakes were characterized by prolonged highstands, lasting several thousand years during the LGM and lasted through the end of the late Pleistocene (~14ka)(e.g., Wells et al., 2003; Anderson and Wells, 2003; Quade et al., 2003). Although there is abundant evidence to suggest that the Holocene of western North America has been drier than the preceding 100 ky, recent paleoclimate studies in southern California suggest that, although the LGM was likely wetter than today, the time interval from 26-18ka was characterized by drier conditions than the previous 10-15 ky (Kirby et al., 2006). If this is confirmed, the Qp erosion surface may be the result of decreased precipitation in the study area during the LGM and attainment of “type 1 stream equilibrium” (Bull, 1990), where tectonic uplift and fluvial downcutting were balanced. This decrease would have resulted in decreased sediment transport capacity of streams, armoring of stream bottoms, and perhaps development of braided stream system; a mechanism proposed by numerous researchers as a means of widening valley bottoms and production of large pediment surfaces (e.g., Ritter, 1967; Bull, 1990). Equilibrium was likely maintained through the dry period of the LGM, after which a wetter climate resulted in degradation (Fig. 18) and abandonment of the pediment surface.

#### ***Latest Pleistocene Alluvium (Q2)***

Two OSL age dates from the Q2 unit, loosely suggest an episode of aggradation in the study area that began sometime before 12.6 ka and ended by ~4.8 ka (Table 1). It is difficult to fully characterize the temporal and spatial patterns of deposition of these deposits because we only have two data points, that are separated by ~8 km in space and 8 k.y. in time (Fig 2). If the onset of aggradation in the study area occurred at 12.6 ka, this might suggest the Q2 unit and infilling of incised canyons along South Mountain is the result of climate change related to the Pleistocene-Holocene transition (Fig. 18). Numerous studies have documented aggradation events in the Mojave Desert across this boundary (e.g., Melton, 1965; Ponti, 1985; Wells et al., 1987; Bull, 1991; Harvey et al., 1999). Less common are studies in southern California. However, Bull (1991) documented a sequence of fill terrace in south flowing drainages in the San Gabriel Mountains (Fig. 1), which he interpreted to represent a period of aggradation that began approximately 14 ka and continued until 4 ka. Aggradation is thought to have resulted from a loss of vegetative cover and accelerated hillslope processes, in response to the transition from a wetter Late Pleistocene climate to a relatively dry semi-arid Holocene climate (e.g., Bull and Schick, 1979; Bull, 1991). Strong correspondence to our age dates on the Q2 unit with aggradation in the San Gabriel Mountains and in the Mojave Desert suggests aggradation in this part of the wTR was the result of climate change during the Pleistocene-Holocene transition (Fig. 18).

In addition to distinguishing the timing of aggradation in the study area, the observed space-time relation between our samples from the Q2 unit provide insight into the post-depositional timing of incision at their respective locations. We observed no evidence of higher fill terraces in any of the drainages, nor evidence of degradation of the sediments near the top of the units we sampled, so we are confident the present geomorphic expression of the Q2 represents the maximum fill elevation. Yet, because both sample were collected within 3 m of the top of the Q2 unit, but differed in age by ~8 ka, we must conclude that the transition from aggradation to incision must have varied along strike of South Mountain. If the Q2 unit is the result of climate change as suggested earlier, the local transition from aggradation to incision likely reflects a change in the local tectonics. The end of deposition and the onset of incision at the eastern older (~12 ka) may reflect folding along the Long Canyon anticline that deforms the south limb of South Mountain (Fig. 2). It is difficult without additional geochronology to know whether the 4 ka age at the western site is indicative of uplift along this part of South Mountain or merely the stabilization of hillslopes, the end of the aggradation, and the return of tectonically controlled incision at this locality.

## **Middle to Late Pleistocene Deformation**

At present, we are unable to constrain the precise timing of deformation on discrete structures within the CFB. However, based on our geologic mapping, geochronology investigation, and GIS-based analysis we are able to bracket the deformational timing on several of the active folds and faults, and develop a relative chronology of deformation. For completeness, we also utilize timing constraints by previous researchers on the timing of deformation north of the CFB along South Mountain and Oak Ridge. We assume the ages on folded terrestrial strata closely approximates the timing of inception of tectonic deformation at discrete localities. This is validated by our OSL dates from Trench 3 on the Camarillo anticline (Fig. 10) that show tectonic colluvial packages, which overlie fluvial strata, are indistinguishable in age and therefore there is no lapse in time between the end of deposition and the onset of tectonic deformation (Table 1). Figure 19 illustrates the approximate initiation time of deformation on previously discussed folds and faults.

Although it is not known if all the Quaternary faults in the study area are characterized by Miocene deformation, faults known to be reactivated are shown in Figure 18a. Hangingwall and footwall cut-off angles in the Sespe, Conejo and Topanga Formations across Miocene structures are typically close to 90°, suggesting Miocene normal faults were likely near vertical and probably accommodated some component of strike-slip motion and vertical-axis rotation. Post-Miocene horizontal-axis rotation and transpressive deformation resulted in a series of steeply-dipping Quaternary reverse and strike-slip faults.

The oldest evidence for Pleistocene folding in the study area is in the vicinity of the Oak Ridge and Big Mountain (Fig. 18b). There the Saugus Formation is deposited on a tilted section of pre-Pliocene bedrock on the south limb of the Big Mountain anticline, is conformable on the north limb with Pliocene Pico Formation, and thickens into the Happy Camp syncline to the north (Fig. 2). Conformity with the Pico Formation on the north limb of the anticline suggests the unconformity on the south limb is the result of Miocene transtensional deformation and is not related to Plio-Pleistocene transpressive folding. Uplift of Big Mountain and down warping of the Happy Camp syncline must have began after deposition of the base of the Saugus Formation. Although the precise age of the base of the Saugus Formation is not known at this locality, it is probably ~780 ka based on the biostratigraphic age from Moorpark Mammoth site, which is near the base of the section. Folding in the Big Mountain area may have began as early as ~780 ka and no later than deposition of the top of the Saugus (200-400 ka)(Fig. 19b).

Uplift of South Mountain began sometime after 200-400 ka (Fig. 19c)(Yeats, 1988; Azor et al., 2002). To the south, in the hangingwall of the north-dipping Simi fault, anticlinal folds within the Sespe and Topanga Formations are juxtaposed across the East Baranca fault, against Pleistocene marine and terrestrial strata (Figs. 19c & 11). Truncation of the Las Posas Sand to the west and its absence to the east suggests the East Baranca fault was active either during or after the time of marine deposition in this part of the basin (450-750 ka). The fault appears to have limited the westward growth of the western Simi anticline and accommodated up-to-the east displacement (Fig. 19c). The East Baranca fault was later cut by the southern strand of the Simi fault. This resulted in growth of the Las Posas anticline following deposition of a thin veneer of terrestrial sediments (Q5) in the Las Posas Hills, inferred to be <200 ka (Fig. 19d). Estimates of fault slip rates for the Simi fault system are between 1.1 mm/yr and 1.5 mm/yr based on other rates within the CFB (Table 2).

It is difficult to say when the onset of folding in the Camarillo Hills began, however, the degree of dissection suggests deformation is coeval to younger than growth of the Las Posas anticline and slip on the Simi fault system (Fig 16 and 17). We have one pending OSL date from the terrestrial strata on the north flank of the Camarillo Hills anticline, but until the analysis is complete we can only estimate the age of these deformed strata. Age estimates based on slip rates suggest Q5 in this area is between 100 and 150 ka (Table 2) (Fig. 18d).

Anticlinal folding and displacement on the Southern Springville fault is younger than 45 ka (Fig. 19e and Table 2). More youthful deformation on the southern strand of the Springville fault relative to the northern strand is further supported by our topographic analysis (Figs. 16b and 17b) and the youthful geomorphic expression of the Springville anticline. Latest Pleistocene fault slip rates on the southern Springville fault are estimated to be at least 1.6 mm/yr (Table 2). Both the Springville and South Mountain anticline terminate at the approximate location of the Wright Road fault. The Wright Road fault deforms Holocene sediments of the Oxnard plain and has up-to-the east sense of displacement and has similar rates of uplift as the southern Springville fault (Table 2). The Wright Road fault is in the approximate location where the on-land segment of the Oak Ridge fault turns southward and becomes dominantly a strike-slip fault (Nicholson, personal comm., 2008). We believe the Wright Road fault is related to this change in style of faulting and limits the westward lateral growth of the Springville fault into the Oxnard plain (Fig. 19e). Estimates of the vertical uplift rate along the Wright Road fault, based on the basal age of Q2, suggests a similar rate of uplift as on the southern Springville fault.

We interpret the youngest folds in the fold belt to be those that deform the youngest deposits (<30ka) and those characterized by weakly dissected uplifted surfaces (Fig. 19f). Within the Santa Rosa Domain, in the hangingwall of the Santa Rosa Valley fault, the Q3p surface is uplifted ~35 m above Calleguas Creek. Because changes in channel lithology cannot account for the 12 m increase in separation between Calleguas creek and the Q3p surface across the Camarosa fault (Fig. 13), we infer the increased downcutting is in response to increased uplift in the Santa Rosa Domain. This indicates a post-23ka increase of 0.43 mm/yr in the uplift rate westward along the Las Posas hills.

The maximum relief along the Camarillo anticline at its eastern extent is ~24 m and decreases westward to ~12 m at the site of the paleoseismic trenches. Interpreted colluvial packages and interpreted soil ages suggest uplift began approximately 27 ka, while deposition of fluvial strata was still ongoing at the western trench site (Fig. 18). This suggests a westward propagation of faulting and folding or a westward decrease in the rate of deformation and erosional beveling along the crest to the west. Given the evidence in both trenches for syntectonic beveling of the anticlinal crest neither interpretation can be invalidated. Therefore we calculate a maximum slip uplift rate of ~1.1 mm/yr based on the maximum relief and youngest deformed sediment (Table 2).

## CONCLUSIONS

This research represents an integrated application of geochronology, geology, and GIS-based analyses, which brackets the timing of deformation on active folding within the CFB, places temporal constraints on the age of deformed terrestrial strata, and develops the Quaternary chronology of landscape evolution for this part of the wTR. We utilize OSL and radiocarbon dates to show the age of terrestrial strata within the CFB are as young as ~25 ky. Strata in the CFB, previously mapped as Saugus Formation, are derived from the Santa Monica Mountains and the Oak Ridge/South Mountain uplift, and not the San Gabriel Mountains as previously suggested. Because uplift of the South Mountain area did not begin until 200-400 ka, all of the terrestrial strata in the CFB are younger than the upper age limit of Saugus strata to the north and east. Our age estimates suggest terrestrial sedimentation did not begin in the CFB until ~160 ka. Deposition of genetically related deposits have been modulated through time by local tectonics and climate forcings and likely continues into the present in the Oxnard plain.

The latest Pleistocene to Holocene landscape of this region of the wTR was characterized by lateral planation of Oligocene to Pleistocene bedrock, followed by deep incision and aggradation. We interpret these changes as the result of climate change over the past 30 ky. Lateral planation of a regionally extensive pediment surface (Q3p) occurred between 26-18 ka, contemporaneous with Oxygen Isotope Stage 2 (OIS2). The Q3p surface is interpreted to be the result of “type 1 dynamic equilibrium” (Bull, 1990) attained during the climate regime related to the Last Glacial Maximum (LGM). The surface is

preserved on the south flank of Big Mountain near Moorpark and as isolated strath terraces along Calleguas Creek. Between ~18-14 ka, subsequent warmer and wetter interstadial climate resulted in incision and abandonment of the Q3p surface and deep canyons were cut into the south flank of the Oak Ridge-South Mountain uplift. Transition to a semi-arid climate following the end of the Pleistocene, resulted in accumulation of a thick (~20 m) section of hillslope-derived sediments (Q2) that back-filled topographic and structural within the study area. These deposits are now being incised in the modern drainages.

Late Quaternary contractional deformation in the CFB is largely accommodated on reactivated Miocene normal faults. North-striking transverse faults, some of which are inherited structures, have limited the lateral growth of faults and folds within the study area. Distinct changes in the magnitude, timing, rate, loci, orientation, and geometry of deformation across transverse faults indicate these faults impede deformation, which has obvious implication to seismic hazard assessment. Locally, transverse faults are cut by east-striking reverse faults. This observation demonstrates transverse faults have a finite strength and may have a temporally-limit role in accommodating lateral propagation and deformation. Systematic decreases in structural relief and degree of topographic modification across any one transverse fault indicates adjacent structural domains young to the west. Holistically, folds within the CFB have grown within the last 200 ky and young to the south and west. Deformation along several of the active structures indicates vertical uplift rates between 1 mm/yr and 1.5 mm/yr. For the southern Simi fault, which is the oldest, longest, most continuous structure, with the greatest magnitude of deformation, we estimate a maximum earthquake moment magnitude of  $M_w = 6.4$ .

Table 1. Geochronology table of all Optically Stimulated Luminescence and Radiocarbon analyses.

| Age (ka)             | Location              | Sample  | Method   | Unit | Description  |
|----------------------|-----------------------|---------|----------|------|--|
| 20.11±2.9            | Camarillo anticline   | 01OSL07 | OSL      | Q3a  | Thin-bedded 1m thick red-brown coarse-grained sandy silt with clay and minor gravel oriented N88W 36SE . 3m downsection of 02OSL07 and 3 m below ground surface  |
| 25.83±4.12           | Camarillo anticline   | 02OSL07 | OSL      | Q3a  | Thin-bedded 1m thick red-brown coarse-grained sand with gravel oriented N88W 36SE. 3 m upsection of 01OSL07 and 3m below ground surface in Earth Systems paleoseismic trench.  |
| 32.27±6.29           | Camarillo anticline   | 03OSL07 | OSL      | Q3a  | Massive flat-lying dark-brown to slightly red-brown very fine-grained sandy silt with cobbles. Collected 3m below ground surface in Earth systems paleoseismic trench.   |
| 27.79±2.28           | Camarillo anticline   | 04OSL07 | OSL      | Q3a  | Well-laminated Yellow-brown fine-grained well-sorted sand lense oriented N80W 36SE, that is truncated upsection by grey-brown massive clay-rich bed. Collected ~7.5 m below ground surface in Geosoils trench.   |
| 29.15±7.71           | Camarillo anticline   | 05OSL07 | OSL      | Q3a  | Upper massive reddish-brown clay-rich bed 1.5 meters upsection of sample site 04OSL07. Unit characterizes the uppermost tilted strata in the trench, is oriented N82W 35SE and interpreted by Geosoils consultants to be a colluvial wedge resulting from tectonic uplift and folding. Collected ~7.5 m below ground surface in paleoseismic trench. |
| 29.73±2.83           | Camarillo anticline   | 06OSL07 | OSL      | Q3a  | Collected ~6cm downsection sample 05OSL07 within the same clay-rich bed.   |
| 40.76±3.81           | Camarillo anticline   | 07OSL07 | OSL      | Q3a  | Massive lower gray-brown clay-rich bed, between samples sites 04OSL07 and 06OSL07. Also interpreted by Geosoils consultants to be a colluvial wedge resulting from tectonic uplift and folding. Collected ~7.5 m below ground surface.   |
| 18.26±1.76           | Camarillo anticline   | 08OSL07 | OSL      | Q1   | Massive flat-lying reddish brown clay-rich bed that overlies flat-lying fluvial sand at the southernmost extent of the Geosoils paleoseismic trench.   |
| 34.39±9.96           | Springville anticline | 09OSL07 | OSL      | Q4   | Trough cross-bedded well-sorted medium-grained sand oriented N45W 12SW. Sample was collected 30cm upsection from sample 10OSL07 within an agricultural cut ~5m below the ground surface.   |
| >46 <sup>a</sup>     | Springville anticline | 10OSL07 | OSL      | Q1   | Massive poorly sorted yellow-brown silty-sand with pebbles exposed in agricultural cut, ~5m down from ground surface and 30cm above sample 10OSL07   |
| 450-700 <sup>b</sup> | Upland Ridge          |         | AAR      | QTlp | Marine fossils collected from the Las Posas sand.  |
| 700 <sup>c</sup>     | North of Moorpark     |         | Biostrat | Qs   | Moorpark Mammoth site. Age date from biostratigraphic correlation of mammal rodent teeth collected at the site.  |

| Age (ka)                | Location                               | Sample  | Method | Unit | Description   |
|-------------------------|--|---------|--------|------|---|
| 26.92±4.06              | North of Somis                         | 12OSL07 | OSL    | Q3p  | Flat-lying massive reddish moderately-sorted pebble-bearing medium-fine-grained sand underlying a sandy well-rounded cobble conglomerate. Sample collected 1.2m below ground surface and exposed in a road cut.                       |
| 24.69±1.98              | East of Moorpark along Calleguas Creek | 13OSL07 | OSL    | Q3p  | Falt-lying massive brown medium-grained sand intrerbedded with cobble conglomerate exposed in railroad cut. Sample was collected 2m below ground surface and 3.5m above erosion surface cut on Oligocene Sespe Formation.             |
| 19.24±1.88              | South flank of Big Mountain anticline  | 18OSL07 | OSL    | Q3p  | Flat-lying trough cross-bedded well-sorted 1.5m thick medium-grained sand bed interbedded with cobble conlomerate. Sample collected 3m downsection from ground surface and 2m above erosion sufrace cut on Oligocene Sespe Formation. |
| 23.28±1.04 <sup>d</sup> | North of the Santa Rosa Valley fault   | RC      | RC     | Q3p  | Sample Collected from fine-grained sediments in consulting trench that have been faulted and uplifted approximately 15m along the Santa Rosa Valley fault.  |
| 12.6±1.38               | Old Balcom Canyon Rd.                  | 17OSL07 | OSL    | Q2   | Massive thick-bedded yellow-green muddy silt containing small clasts of Monterey shale. Sample collected 4m down from ground surface.   |
| 4.78±0.47               | West Las Posas Valley                  | 19OSL07 | OSL    | Q3   | Massive thick-bedded yellow-green muddy silt containing small clasts of Monterey shale. Sample collected 3m down from ground surface.   |
| 0.94±0.04               | Oxnard Plain                           | 04RC07  | RC     | Q1   | Collected from dark brown to black overbank clay along Beardsley Creek aproximately 1.5 down form grounds surface.  |

Table 2. Seismic sources of the Camarillo Fold Belt, with fault dimensions, activity, vertical rate, and max moment magnitude determined using the methodology of Wells and Coppersmith (1994)

| Fault  | Anticline(s)       | Length <sup>a</sup><br>(km) | Slip                      | Vertical<br>Offset<br>(m) | Age of offset<br>datum (ka.) | Vertical rate of<br>faulting (mm/yr) | Activity <sup>b</sup> | Max (M <sub>w</sub> ) <sup>c</sup> | Max (M <sub>w</sub> ) <sup>d</sup> |
|--|--------------------|-----------------------------|---------------------------|---------------------------|------------------------------|--------------------------------------|-----------------------|------------------------------------|------------------------------------|
| <i>Simi Fault System</i>                     |                    |                             |                           |                           |                              |                                      |                       |                                    |                                    |
| NE. Simi segment                             | Las Posas          | 3.8                         | Reverse                   | 35                        | 107-160 <sup>e</sup>         | N/A                                  | PA                    | 5.7                                | 5.2                                |
| NW. Simi segment                             | Las Posas          | 3.5                         | Reverse                   | 60                        | 107-160 <sup>e</sup>         | N/A                                  | AA                    | 5.7                                | 5.2                                |
| Southern Simi                                | Simi and Las Posas | 24                          | Oblique Left-<br>Reverse  | 111                       | 107-160 <sup>e</sup>         | N/A                                  | A                     | 6.5                                | 6.4                                |
| <i>Santa Rosa Fault System</i>               |                    |                             |                           |                           |                              |                                      |                       |                                    |                                    |
| N. Santa Rosa                                | Upland Ridge       | 3.8                         | Reverse                   | ~25                       | 83-125e                      | N/A                                  | AA                    | 5.7                                | 5.2                                |
| C. Santa Rosa                                | Upland Ridge       | 2.8                         | Oblique Left-<br>Reverse  | ~25                       | 83-125e                      | N/A                                  | AA                    | 5.6                                | 5                                  |
| S. Santa Rosa                                | Upland Ridge       | 4.4                         | Reverse                   | 75                        | 83-125 <sup>e</sup>          | N/A                                  | AA                    | 5.7                                | 5.3                                |
| Santa Rosa Valley                            | Santa Rosa Valley  | 4.8                         | Reverse                   | 35                        | 23                           | 1.5                                  | AA                    | 5.8                                | 5.4                                |
| <i>Springville Fault System</i>              |                    |                             |                           |                           |                              |                                      |                       |                                    |                                    |
| )  | Camarillo Hills    | 6                           | Reverse                   | 152                       | 100-150 <sup>e</sup>         | N/A                                  | AA                    | Coseismic                          | Coseismic                          |
| N. Springville B                             | Camarillo Hills    | 6                           | Reverse                   | 152                       | 100-150 <sup>e</sup>         | N/A                                  | AA                    | 5.9                                | 5.5                                |
| S. Springville                               | Springville        | 3.5                         | Reverse                   | 75                        | 45                           | 1.6                                  | A                     | 5.7                                | 5.2                                |
| <i>Camarillo Fault System</i>                |                    |                             |                           |                           |                              |                                      |                       |                                    |                                    |
| Camarillo                                    | Camarillo          | >5.5                        | Reverse                   | 24                        | 22                           | 1.1                                  | AA                    | 5.8                                | 5.5                                |
| <i>North Striking Transverse Tear Faults</i> |                    |                             |                           |                           |                              |                                      |                       |                                    |                                    |
| E. Baranca Rd.                               |                    | >3                          | Oblique Right-<br>Reverse | inactive                  | N/A                          | 0.00                                 | inactive              | Coseismic                          | Coseismic                          |
| Camarosa                                     |                    | >4.5                        | Oblique Right-<br>Reverse | 94                        | 100-150 <sup>e</sup>         | 0.2 - 0.1                            | PA                    | Coseismic                          | Coseismic                          |
| Somis  |                    | 6.5                         | Oblique Right-<br>Reverse | 79                        |                              | 0.2 - 0.1                            | PA                    | Coseismic                          | Coseismic                          |
| Wright Rd.                                   |                    | >7.5                        | Oblique Right-<br>Reverse | 20                        | 12.6                         | 1.6                                  | AA                    | Coseismic                          | Coseismic                          |

a. Fault length is assumed to be the surface rupture length and may be slightly different than map length

b. A = Active: demonstrated Holocene (11,500 B.P.); AA = Apparently Active: very young (Probably Holocene) topographic expression of activity; PA = Potentially Active: Active in Pleistocene (last 1.8 m.y.)

c. Moment Magnitude estimation based on rupture area with and assumed fault depth of 12 km.

d. Moment Magnitude estimation based on on rupture length.

e. Inferred age based on a slip rate of 1.0-1.5 mm/yr



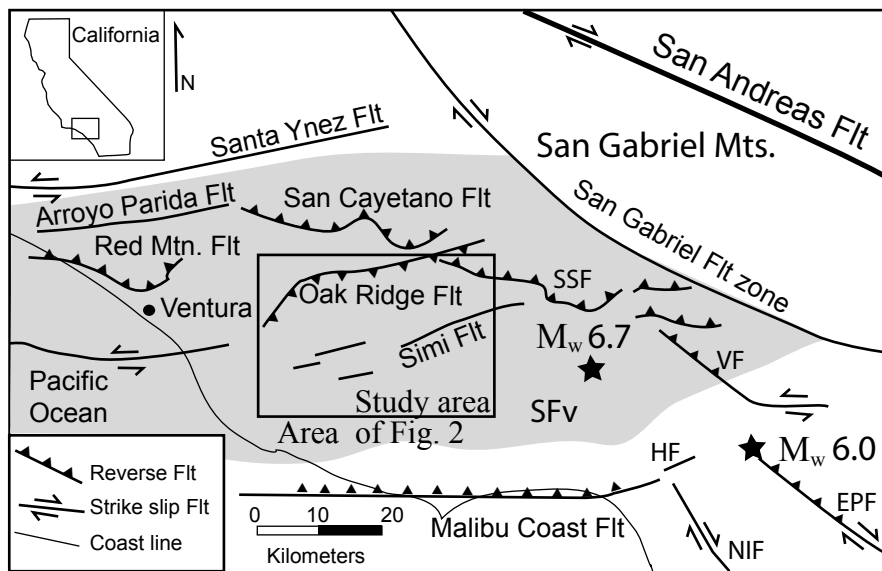


Figure 1.  
Index map of the principle active faults in southern California with respect to the study area. Shaded area shows the location of the Mio-Pliocene Ventura basin. Location of the 1987 Mw 6.0 Whittier Narrows and 1994 Mw 6.7 Northridge earthquakes are shown as black stars. SSF-Santa Susana Fault; VF-Verdugo Fault; NIF-Newport-Inglewood Fault; EPF-Elsinore/Puente Hills Fault; SFv-San Fernando Valley.

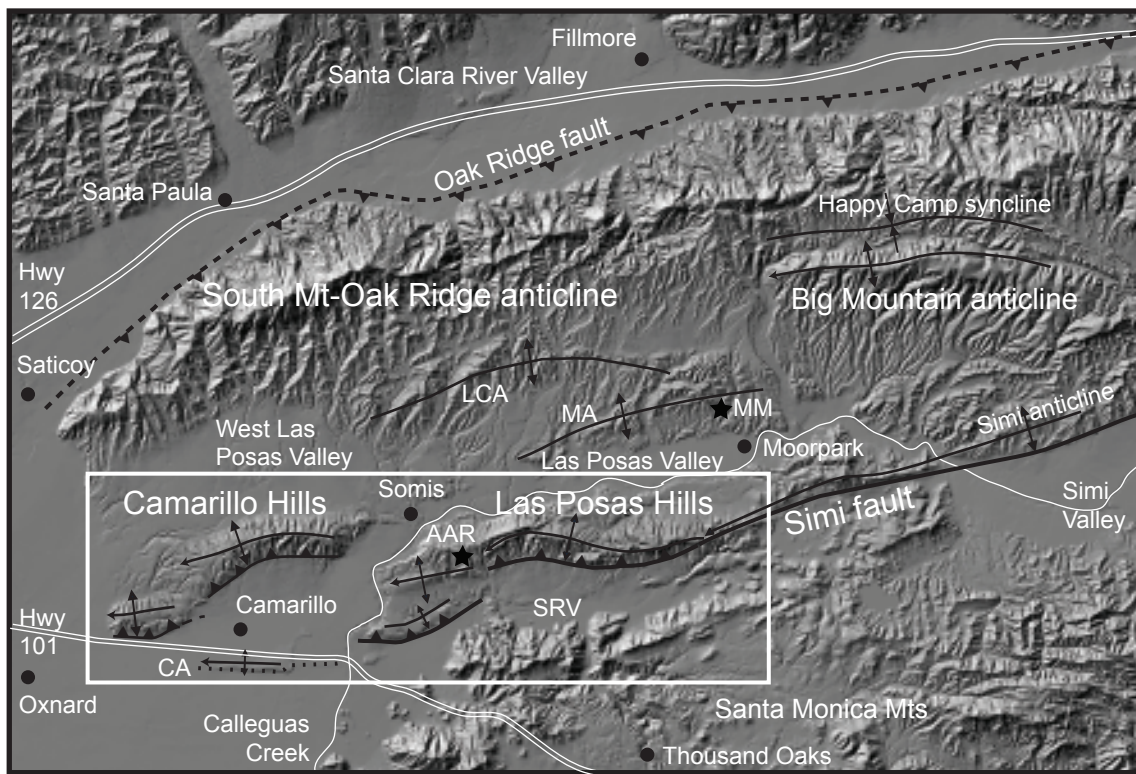


Figure 2.

Shaded relief map showing the important faults and folds that accommodate north-south contraction and illustrating the dominant east-west structural grain of this part of the wTR. The white box shows the area of the CFB and the approximate location of Figures 6 and 11.

AAR-Amino Acid Racimization age date; CA-Camarillo Anticline; MM-Moorpark Mammoth site; SRV-Santa Rosa Valley.

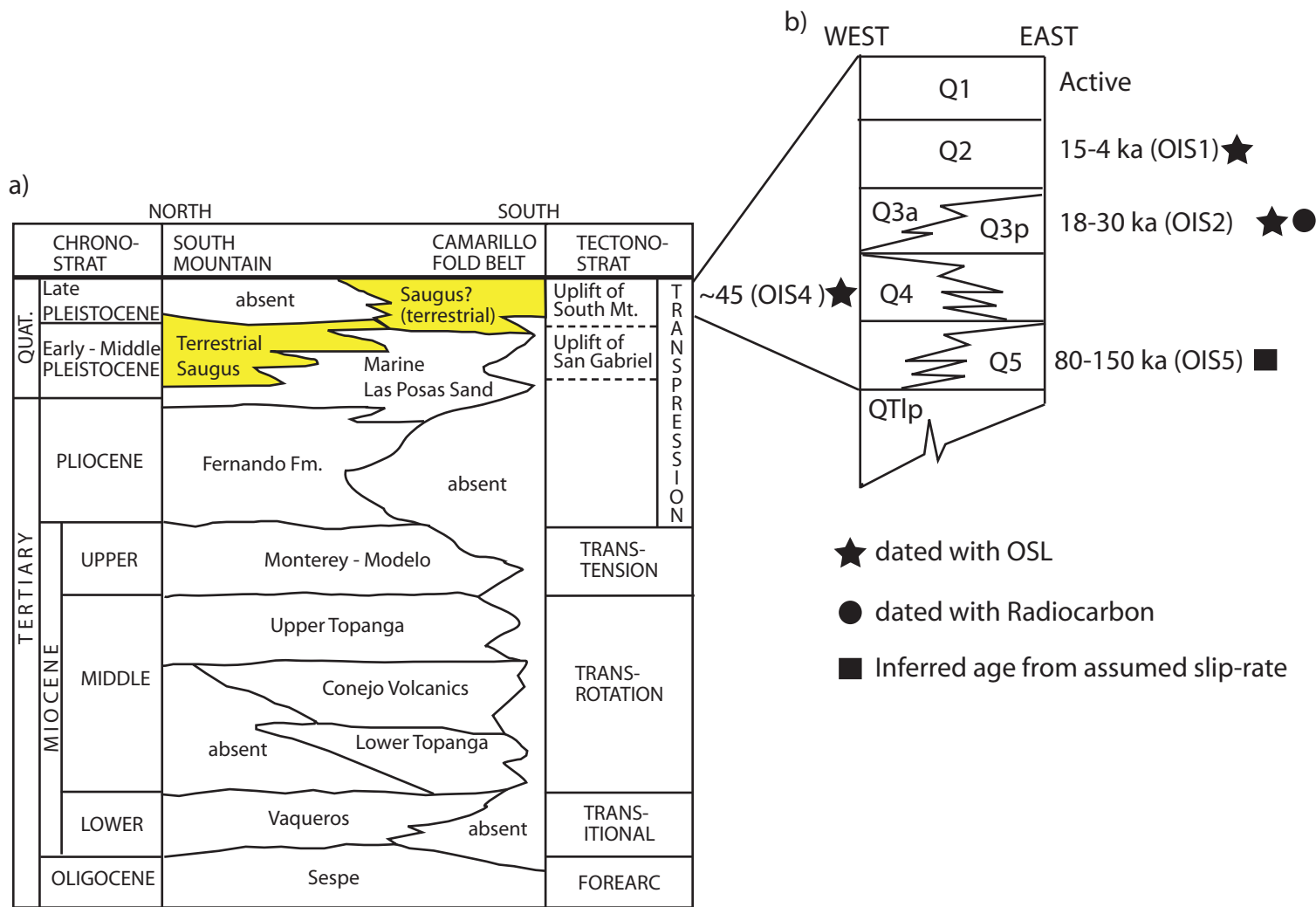


Figure 3.

Stratigraphic column of Oligocene to Holocene strata in the western Transverse Ranges. a) Column illustrating the north to south stratigraphic variability between South Mountain to the north and the CFB to the south. Plio-Pleistocene formation in the CFB unconformably overlies Oligocene to Miocene strata. The Pliocene Fernando Fm. is absent in the CFB (Modified from Ingersoll, 2001). b) Column illustrating the west to east stratigraphic variability of late Middle Pleistocene to Holocene sediments in the CFB and the nomenclature used for this study. Q5 and Q4 likely characterize a time-transgressive westward younging prograding sequence of terrestrial strata. Q3a and Q3p are coeval and are lateral equivalents with Q3a deposition occurring to the west in a more distal environment than sediments deposited on the Q3p erosion surface.

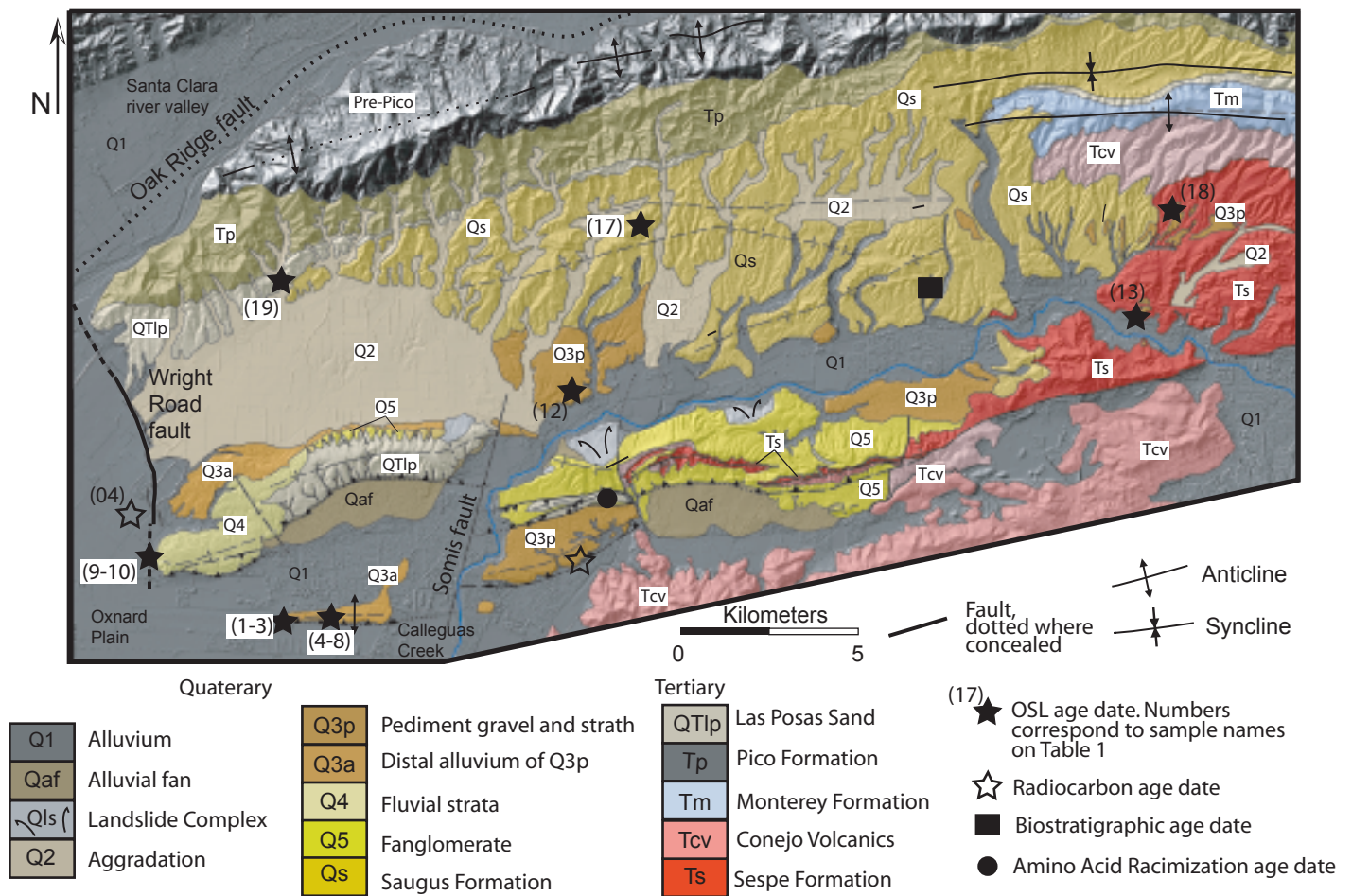


Figure 4.

Generalized geologic map of South Mounatin, the Santa Monica Mts, and the CFB showing the locations of faults, and the distribution of Oligocene to Quaternary lithologic units and locations of absolute age dates (this study and previous studies).

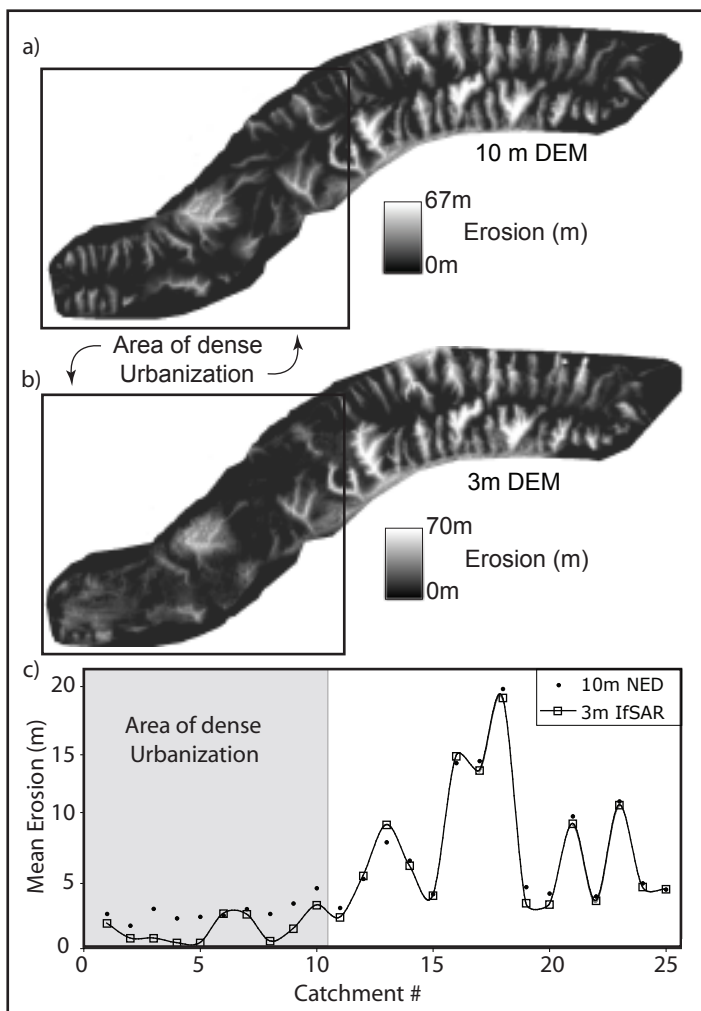


Figure 5.

Two images of the Camarillo Hills showing the magnitude of erosional denudation determined from two different Digital Elevation Model datasets, illustrating the effects of urbanization on calculations of Catchment denudation (Cd). a) 10-m NED dataset. Note well-defined channel networks shown by increased erosion (white) along trunk channels within both urbanized and natural regions of the fold. b) 3-m IfSAR data. Note that the channel network within the urbanized area are poorly defined due to infilling of natural channels. c) Cd data plot from the Camarillo Hills showing the effects of urbanization on the magnitude of denudation. Note that in regions of urbanization 3-m data show a decrease in magnitude of Cd, due to infilling of natural channels, while in areas with less development both datasets are in good agreement.



a)



b)

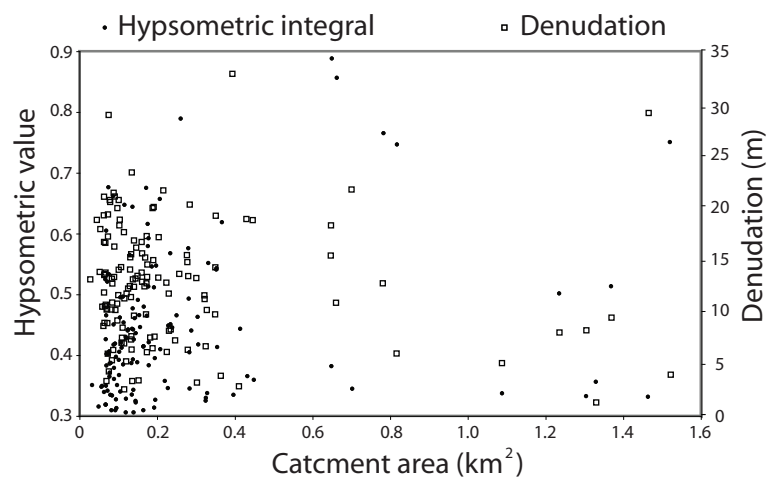


Figure 6.

a) Image of all drainage catchments from both the north and south flanks of folds analyzed for determination of the hypsometric integral and catchment denudation. Not that catchment areas are highly variable and range in size between 0.1 to 1.5  $\text{km}^2$ . b) Compilation of all hypsometry and denudation data plotted against catchment area showing no systematic relationship between area and index value.

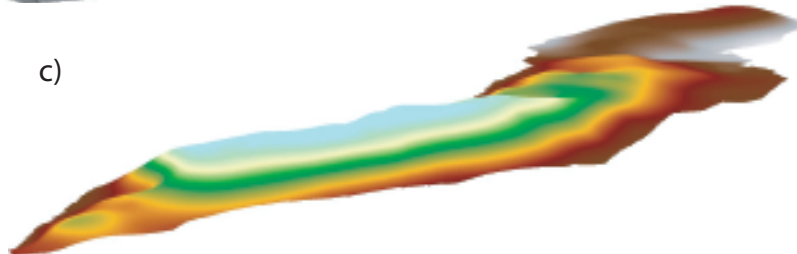
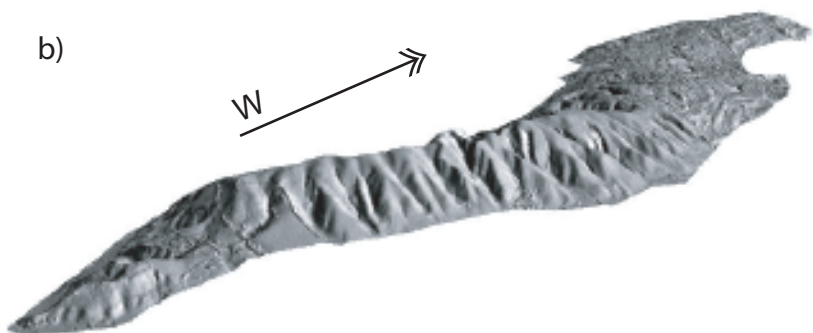
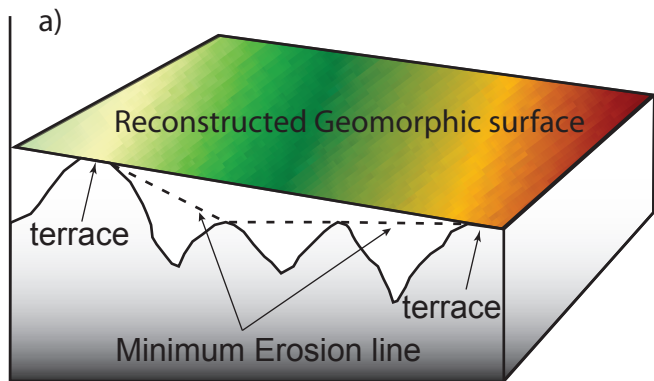


Figure 7.

a) Idealized block diagram showing how catchment denudation is calculated. Where geomorphic surfaces such as fluvial terraces and uneroded dip-slopes are present, catchment denudation can accurately be quantified by subtracting the DEM from the reconstructed geomorphic surface. In the absence of pristine geomorphic surfaces, elevations of drainage divides can be substituted into the interpolated surface calculation, thereby providing a minimum estimate of catchment denudation.

b) Hillshade of the Camarillo Hills (3x V.E.). c) Interpolated surface across the Camarillo Hills. Not the smooth equal elevation color bands around the flank of the fold showing accurate reconstruction of uneroded dip-slopes. However, the uneven appearance at the crest of the hills is the result of erosion indicating calculated valued of denudation are a minimum.

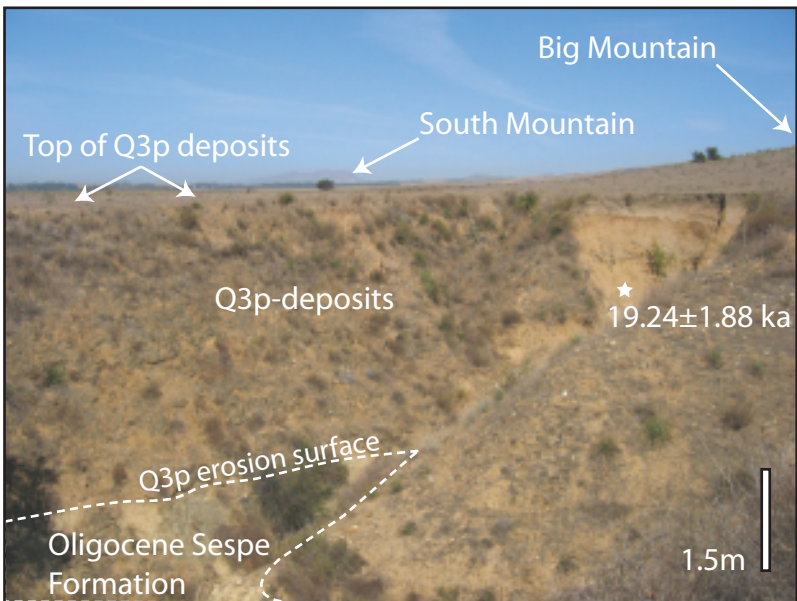


Figure 8.  
Photograph of the Quaternary Pediment surface (Q3P) and overlying gravels (view to the west). Q3p deposits are commonly stripped exposing the near planar bedrock erosion surface. See figure 2 for location of sample 18OSL07 and this photograph.

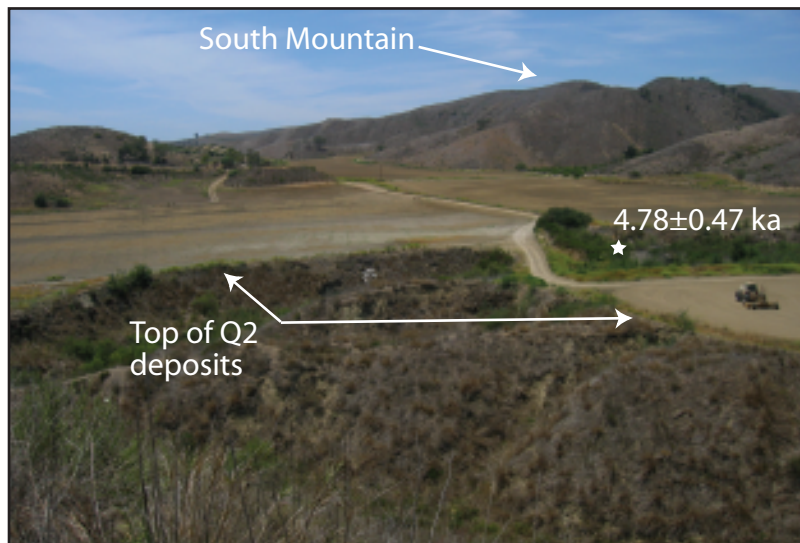


Figure 9.  
Photograph of the Q2 deposits on the south flank of South Mountain (view to the north). Note the broad flat valley floor composed of Q2 deposits that locally extend from the west Las Posas valley to the south to near the topographic highs of South mountain. Q2 deposits fill topographic and structural lows north of the CFB and are locally >20m in thickness. See figure 2 for location of sample site 19OSL07 this photograph.



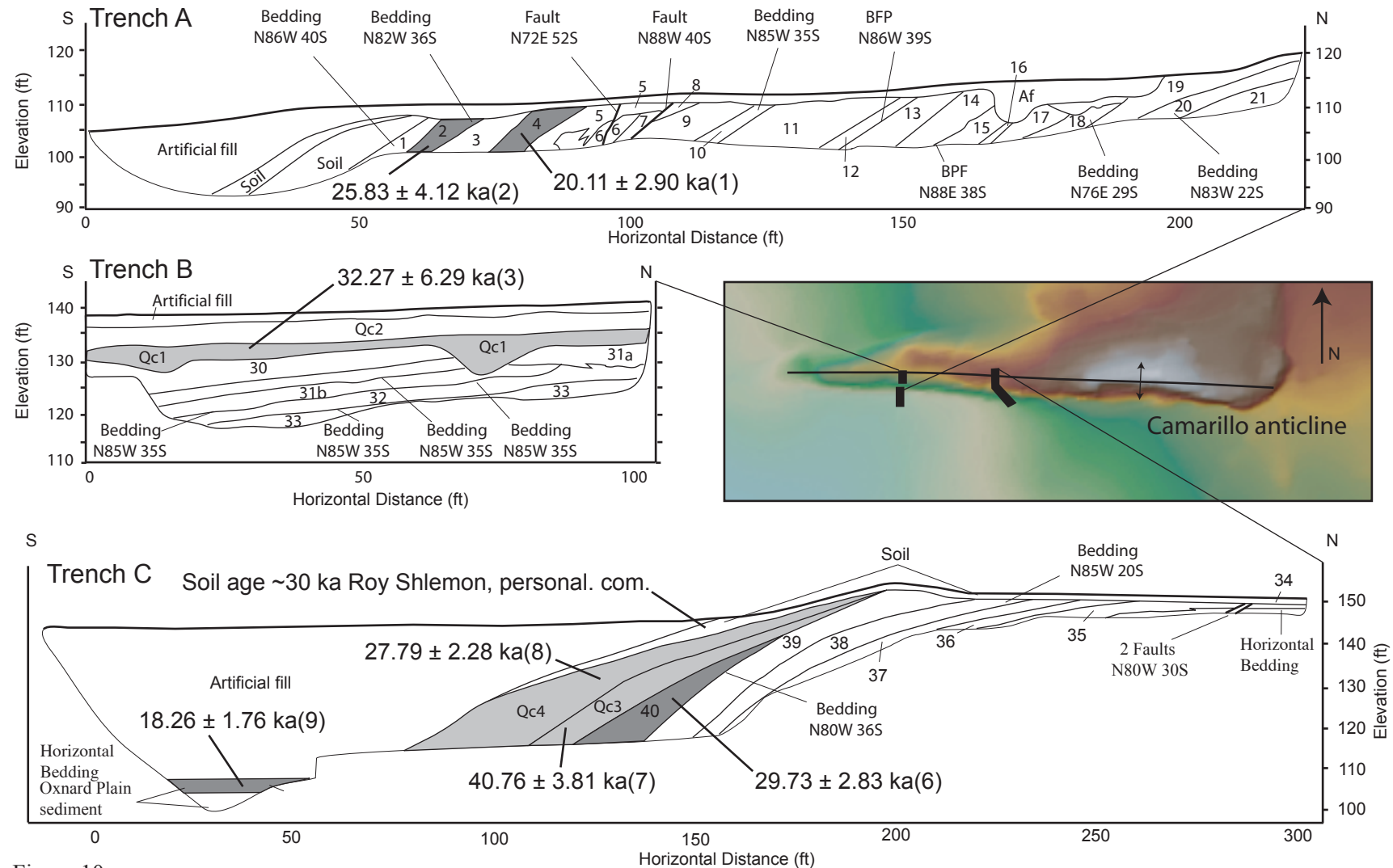


Figure 10. Schematic line drawings of trench logs across the Camarillo fault/fold zone. Inset shows shaded relief map showing the relative position of fault trenches with respect to the axis and topographic expression of the Camarillo anticline (see Figure 2 for location of inset). Numbered units (1-40) are an interbedded sequence of well-sorted fluvial conglomerate, sandstone, and siltstone beds characterized as Saugus Formation in consultant logs (Q3a this study). Dark grey numbered fluvial strata were sampled for OSL dating. Interpreted colluvial units (Qc 1-4) are locally discordant with the underlying fluvial strata and are interpreted to record post-tectonic deposition on a growing fold. Light-gray shaded units reflect Quaternary colluvial packages sampled for OSL dating. Trenches A and B expose several south-dipping faults interpreted as backthrusts or bending moment normal faults. The Camarillo fault was not distinctly encountered in any of the trenches. Deformation along the Camarillo fault zone is best characterized by blind faulting. Age dates are from OSL analysis with numbers in paranthesis corresponding sample numbers in Table 1. Note Trench C is not the same scale as Trenches 1 and 2.

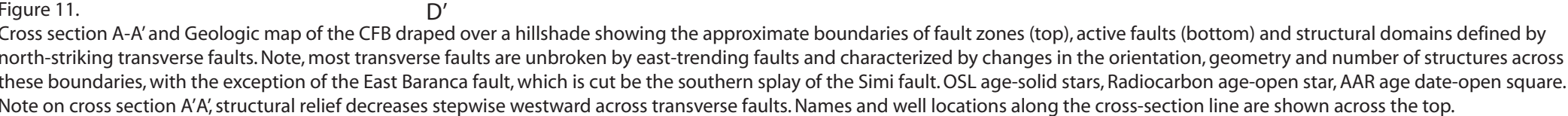


Figure 11. D' Cross section A-A' and Geologic map of the CFB draped over a hillshade showing the approximate boundaries of fault zones (top), active faults (bottom) and structural domains defined by north-striking transverse faults. Note, most transverse faults are unbroken by east-trending faults and characterized by changes in the orientation, geometry and number of structures across these boundaries, with the exception of the East Baranca fault, which is cut by the southern splay of the Simi fault. OSL age-solid stars, Radiocarbon age-open star, AAR age date-open square. Note on cross section A-A', structural relief decreases stepwise westward across transverse faults. Names and well locations along the cross-section line are shown across the top.

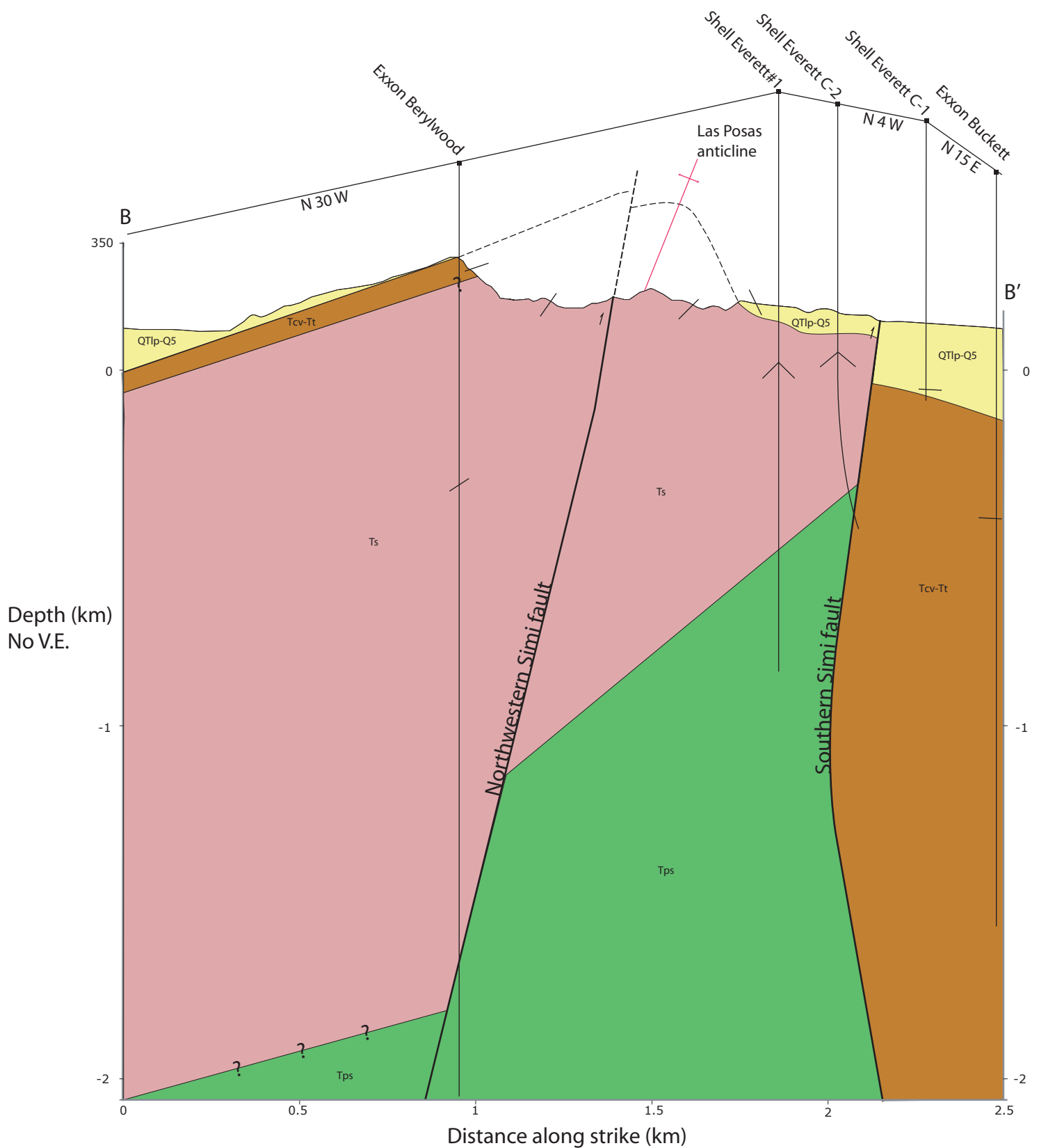


Figure 12.  
Cross section B-B' across the NW and southern Simi fault splays. Note thick section of Tcv-Tt south of the southern splay of the Simi fault indicating Miocene down-to-the-south displacement. Location of crosssection shown on Figure 10. Well names shown across the top.

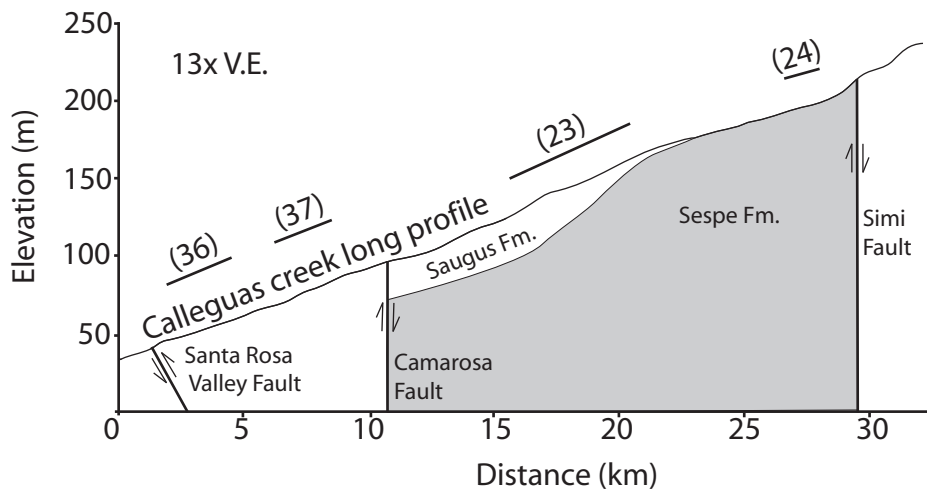


Figure 13.

Long Profile of Calleguas Creek with respect to the Qp surface. The elevational difference between Calleguas Creek and the Q3p surface is in meters and shown in parentheses above the approximate location of the pediment surface with respect to the long profile. After crossing the approximate location of the Camarosa fault, spacing between the two datum increases by ~13 m., which may suggest an increase in post-23 ka uplift west of the fault.

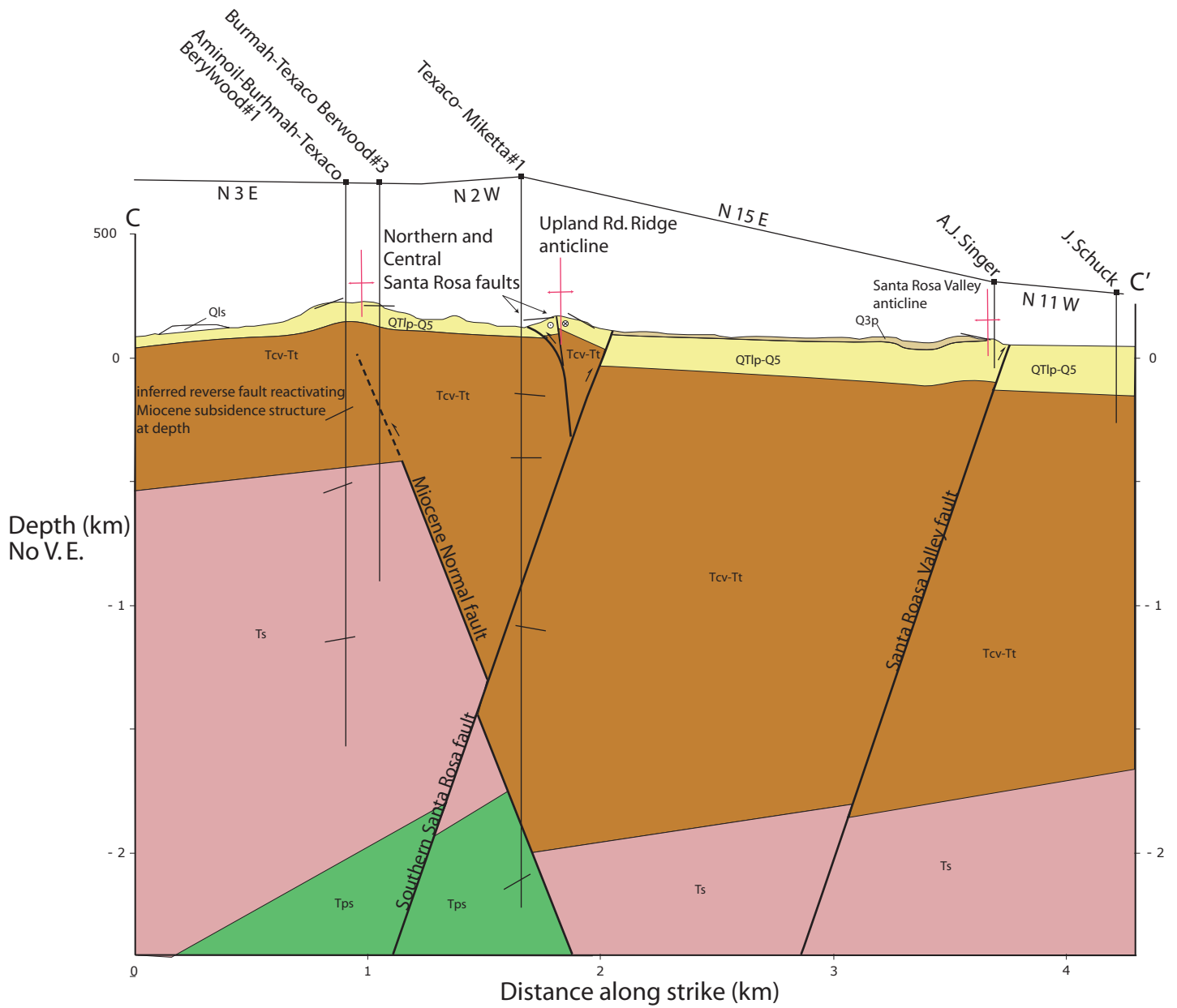


Figure 14.

Cross section C-C' across the NW across the Santa Rosa Domain. Note thickening of QTlp-Qs south of the southern Santa Rosa fault. Location of cross-section shown on Figure 10. Well names shown across the top.

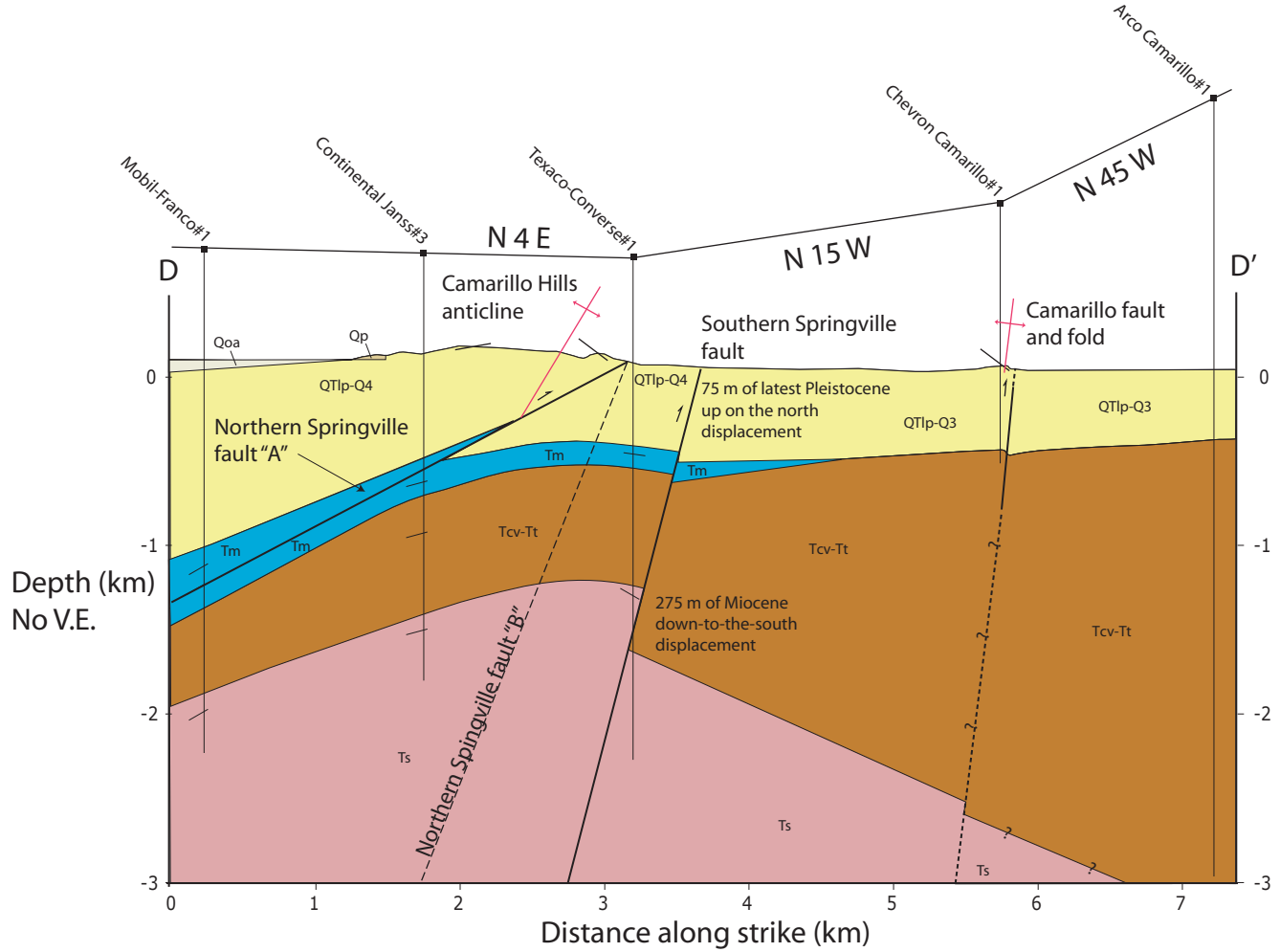


Figure 15.

Cross section D-D' across the Springville and Camarillo fault zones. Note 275 m of down-to the south Miocene displacement of the top of the Sespe Formation, southward thickening of Tcv-Tt and perpendicular footwall cut-off angles. Two fault plane solutions are shown for the northern Springville fault. Solution A dips  $\sim 25^\circ$  and Solution B dips  $\sim 75^\circ$ .

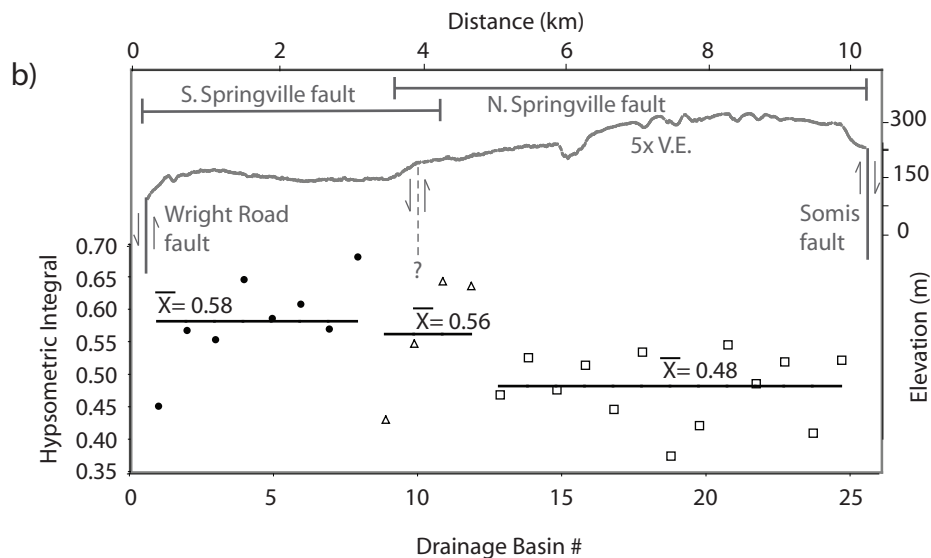
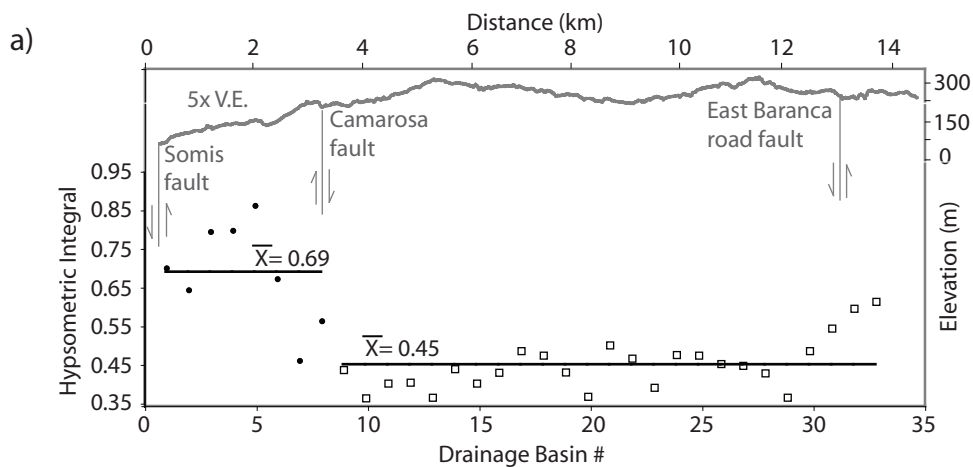


Figure 16.

Hypsometric integral ( $H_i$ ) plots across the CFB. a)  $H_i$  plot of the Simi and Santa Rosa domains. Note distinct changes across the Camarosa fault. b)  $H_i$  plot of the Camarillo Hills-Springville fault zone. Note westward increase in value suggesting westward younging of the fault zone.

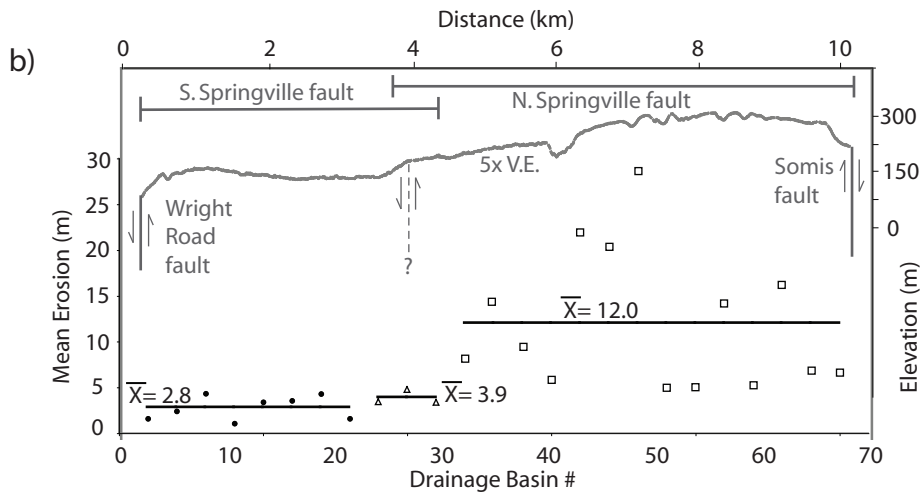
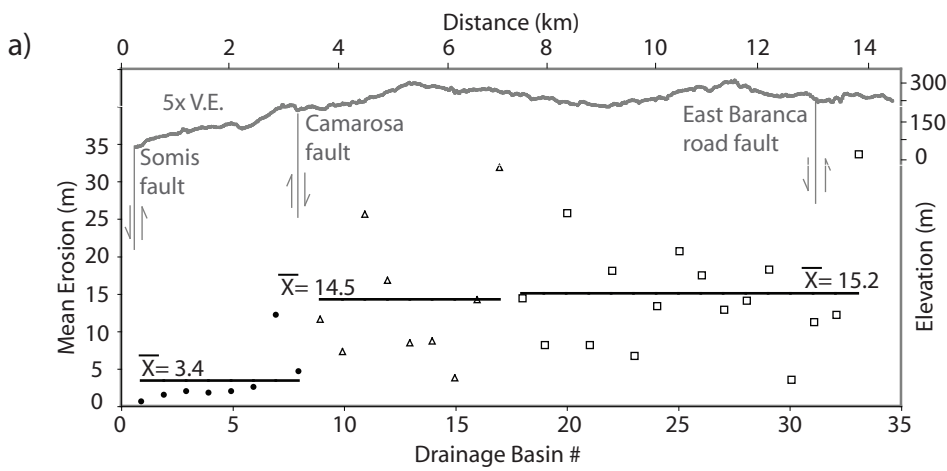


Figure 17.

Denudation plots across the CFB. a) denudation of the Simi and Santa Rosa domains. No obvious changes are observed along the entire length of the southern fault or across the two northern segments. However, across the Camarosa fault a 4x decrease in erosion is observed. b) Denudation plot along the Camarillo Hills-Springville fault zone showing 3x to 4x decrease in erosion between the northern and southern splays of the Springville fault.



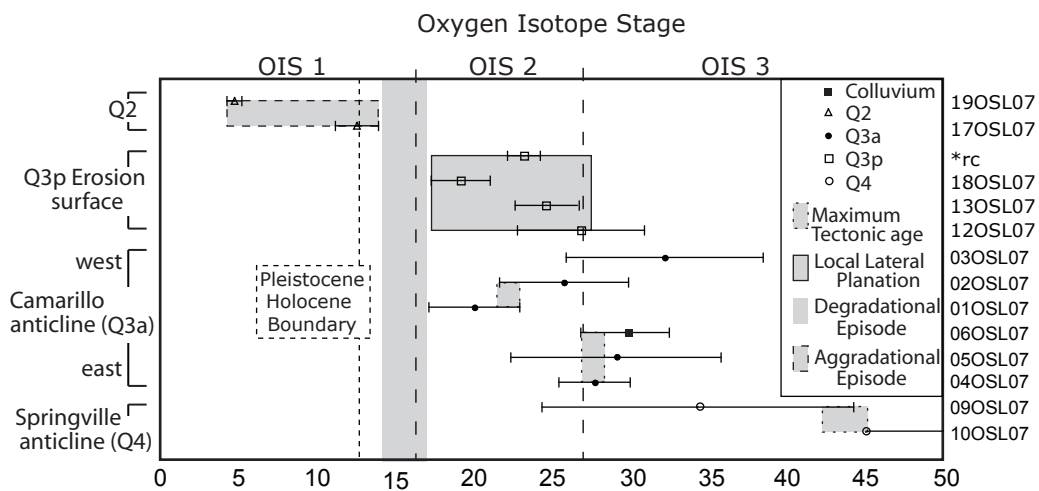


Figure 18.

Interpreted ages of landscape evolution in the CFB and South Mountain with respect to sample location and global climate (Oxygen Isotope stage). We assess a maximum age of tectonic deformation based on the age of the strata deformed within the Springville and Camarillo anticlines. Samples collected from sediment that overlie the Qp erosion surface suggest a range of ages for lateral planation of bedrock between ~26–18 ka correlating to OIS2. Abandonment of the Qp surface and bedrock incision occurred following lateral planation before aggradation event which back-filled paleodrainages and structural lows along the south flank of South Mountain in response to climate change associated with the Pleistocene-Holocene transition.

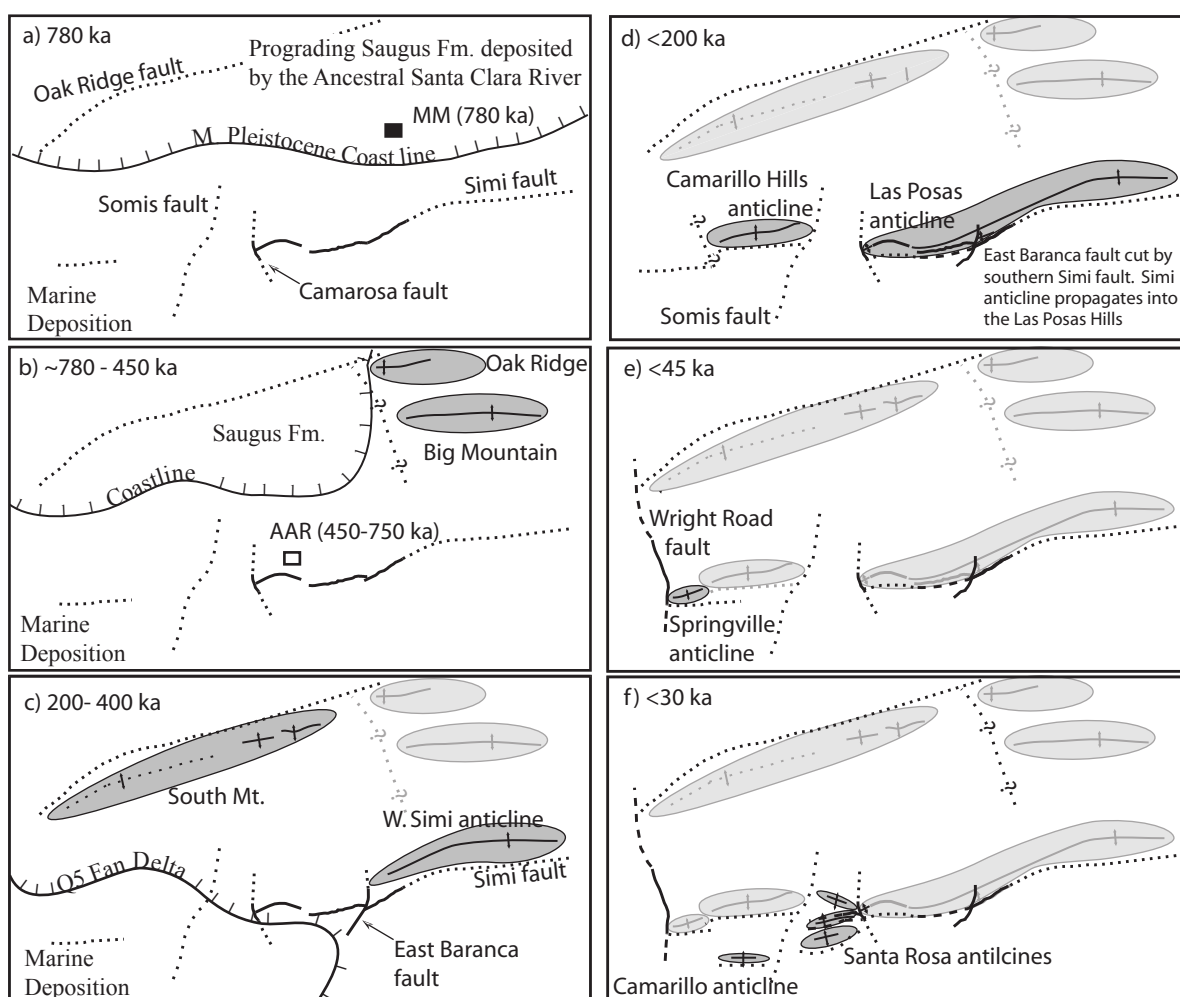


Figure 19. Schematic diagram illustrating important timing of terrestrial sedimentation and fold growth in the study area between ~780 ka to <30 ka. a) Saugus Formation deposited across the future location of the South Mountain and the Oak Ridge uplift, while to the south in the CFB marine deposition continues. Black box illustrates the approximate location of the Moorpark Mammoth site. b) Deformation along the Oak Ridge fault and Big Mountain anticlines begins to isolate the CFB from Saugus sediment sourced in the San Gabriel Mountains. Westward propagation of these folds may have been limited by a hypothesized cross fault. Marine deposition may continue in the CFB until ca. 450 ka based on AAR age date. c) uplift of South Mountain along the Oak Ridge fault (Yeats, 1988) completely isolates the CFB from the Santa Clara river. Sediment shed from uplift along the Oak Ridge fault pushes coastline southward resulting in terrestrial deposition in the CFB. The western Simi anticline propagates to but not beyond the East Baranca fault. d) Simi fault and anticlinal folding propagate westward into the Las Posas Hills/anticline offsetting the East Baranca fault. Uplift of the Camarillo Hills anticline begins west of the Somis fault and terminates to the west at a hypothesized cross fault. e) Springville fault steps southwestward and uplift of the Springville anticline begins. f) Folding in the Santa Rosa area and Camarillo anticline begins. Note regional southwestward propagation of deformation in the study area and westward younging of folds across transverse faults.

## References

- Anderson, D. E., Wells, S.G., 2003, Latest Pleistocene lake highstands in Death Valley, California: Special Paper - Geological Society of America, v. 368, p. 115-128.
- Argus, D. F., Heflin, M. B., Donnellan, A., Webb, F. H., Dong, D., Hurst, K. J., Jefferson, D. C., Lyzenga, G. A., Watkins, M. M., and Zumberge, J. F., 1999, Shortening and thickening of metropolitan Los Angeles measured and inferred by using geodesy: *Geology* (Boulder), v. 27, no. 8, p. 703-706.
- Azor, A., Keller, E.A., and Yeats, R.S., 2002, Geomorphic indicators of active fold growth; South Mountain-Oak Ridge Anticline, Ventura Basin, Southern California: *Geological Society of America Bulletin*, v. 114, p. 745-753.
- Bailey, T.L., 1951, *Geology of a portion of Ventura Basin*: unpublished map
- Blackie, G. W., and Yeats, R. S., 1976, Magnetic-reversal stratigraphy of Pliocene-Pleistocene producing section of Saticoy oil field, Ventura Basin, California: *AAPG Bulletin*, v. 60, no. 11, Part 1, p. 1985-1992.
- Blake, T. F., 1991a, Synopsis of the character and recency of faulting along the Simi-Santa Rosa fault system: in *Engineering Geology along the Simi-Santa Rosa fault system and adjacent areas, Simi Valley to Camarillo Ventura County, California*, in Blake, T. F., ed., *Annual field trip guidebook Southern California Section Association of Engineering Geologists*, v. 1., p. 96-118.
- Blake, T. F., 1991b *Engineering Geology along the Simi-Santa Rosa fault system and adjacent areas, Simi Valley to Camarillo Ventura County, California*. *Annual field trip guidebook Southern California Section Association of Engineering Geologists*, 2v., 383 p.
- Boales, P. V., 1991, Near-surface geology of the southwestern Las Posas Hills area, Camarillo, Ventura County, California, in Blake, T. F., ed., *Engineering Geology along the Simi-Santa Rosa fault system and adjacent areas, Simi Valley to Camarillo Ventura, California*, p. 230-243.
- Brozovic, N. B., D W; Fielding, E J F; Meigs, A J, 1995, The spatial and temporal topographic evolution of Wheeler Ridge, California; new insights from digital elevation data: *Geological Society of America Abstracts with Programs*, v. 27, no. 6, p. 396.
- Buena Engineers, 1987, *Geologic report for Tract 4296, Camarillo, California*, (unpublished consultant report).
- Bull, W. B., and Schick, A. P., 1978, Impact of climatic change on an arid watershed: *Abstracts with Programs - Geological Society of America*, v. 10, no. 3, p. 98.
- Bull, W. B., 1990, Stream-terrace genesis; implications for soil development: *Geomorphology*, v. 3, no. 3-4, p. 351-367.
- Canter, N. W., 1974, *Paleogeology and paleogeography of the Big Mountain area, Santa Susana, Moorpark, and Simi Quadrangles, Ventura County, California*: Ohio University at Athens, Athens, OH, United States (USA).
- Crowell, J. C., 1976, Implications of crustal stretching and shortening of coastal Ventura Basin, California: *Miscellaneous Publication (American Association of Petroleum Geologists Pacific Section)*, no. 24, *Aspects of the geol. hist. of the Calif. Cont. Borderland*, p. 365-382.
- Dibblee, T. W., Ehrenspeck, H. E., Thomas W. Dibblee Jr. Geological Foundation., California. Division of Mines and Geology., and Geological Survey (U.S.), 1990, *Geologic map of the Camarillo and Newbury Park quadrangles, Ventura County, California*: Dibblee Geological Foundation, scale 1:24,000.

- Dibblee, T. W., Ehrenspeck, H. E., California. Division of Mines and Geology., Geological Survey (U.S.), and Thomas W. Dibblee Jr. Geological Foundation., 1992a, Geologic map of the Moorpark quadrangle, Ventura County, California: Dibblee Geological Foundation, scale 1:24,000.
- Dibblee, T. W., Ehrenspeck, H. E., Thomas W. Dibblee Jr. Geological Foundation., California. Division of Mines and Geology., and Geological Survey (U.S.), 1992b, Geologic map of the Simi quadrangle : Ventura County, California: Dibblee Geological Foundation ; Division of Mines and Geology distributor, scale 1:24,000.
- Donnellan, A., Hager, B. H., and King, R. W., 1993, Discrepancy between geological and geodetic deformation rates in the Ventura Basin: *Nature*, v. 366, no. 6453, p. 333-336.
- Dolan, J. F., Christofferson, S. A., and Shaw, J. H., 2003, Recognition of paleoearthquakes on the Puente Hills blind thrust fault, California: *Science*, v. 300, no. 5616, p. 115-118.
- Dolan, J. F., Sieh, K., Rockwell, T. K., Yeats, R. S., Shaw, J., Suppe, J., Huftile, G. J., and Gath, E. M., 1995, Prospects for larger or more frequent earthquakes in the Los Angeles metropolitan region: *Science*, v. 267, no. 5195, p. 199-205.
- Dolan, J. F., Sieh, K., Rockwell, T. K., Gupta, P., and Miller, G., 1997, Active tectonics, paleoseismology, and seismic hazards of the Hollywood fault, northern Los Angeles basin, California: *Geological Society of America Bulletin*, v. 109, no. 12, p. 1595-1616.
- Ehrenspeck, H. E., 1972, Geology and Miocene volcanism of the eastern Conejo Hills area, Ventura County, California [Thesis M A --University of California Santa Barbara 1972 thesis], vii, 135 leaves, bound. p.
- Glenn, D., 1991, A fault trenching study along the Springville fault zone, Camarillo, California, *in* Blake, T. F., ed., *Engineering Geology along the Simi-Santa Rosa fault system and adjacent areas, Simi Valley to Camarillo, Ventura, California*, p. 205.
- Gurrola, L. D., Keller, E. A., and Anonymous, 1999, Seismic hazards of the Santa Barbara fold belt, California: *Abstracts with Programs - Geological Society of America*, v. 31, no. 7, p. 474.
- Gonzalez, T., and Rockwell, T. K., 1991, Holocene activity of the Springville Fault in Camarillo, Transverse Ranges, Southern California; preliminary observations: *in* Blake T. F., ed., *Engineering Geology along the Simi-Santa Rosa fault system and adjacent areas, Simi Valley to Camarillo Ventura County, California*. Annual field trip guidebook Southern California Section Association of Engineering Geologists, v. 2, p. 396-383.
- Gurrola, L. D., Keller, E. A., and Anonymous, 1999, Seismic hazards of the Santa Barbara fold belt, California: *Abstracts with Programs - Geological Society of America*, v. 31, no. 7, p. 474.
- Hancock, G. S., and Anderson, R. S., 2002, Numerical modeling of fluvial strath-terrace formation in response to oscillating climate: *Geological Society of America Bulletin*, v. 114, no. 9, p. 1131-1142.
- Hanson, D. W., 1982, Surface and subsurface geology of the Simi Valley area, Ventura County, California: Oregon State University, Corvallis, OR, United States (USA).
- Hanson, R.T., Martin, P., Kocot, K.M., 2003, Simulation of Ground-Water/Surface-Water Flow in the Santa Clara-Calleguas Ground-Water Basin, Ventura County, California, U.S. Geological Survey Water Resources Report, 157 p.
- Hauksson, E., Jones, L. M., and Hutton, K., 1995, The 1994 Northridge Earthquake Sequence in California - Seismological and Tectonic Aspects: *Journal of Geophysical Research-Solid*

- Earth, v. 100, no. B7, p. 12335-12355.
- Hitchcock, C. S., Treiman, J. A., Lettis, W. R., Simpson, G. D., and Anonymous, 1998, Paleoseismic investigation of the Simi Fault at Arroyo Simi, Simi Valley, Ventura County, California: Abstracts with Programs - Geological Society of America, v. 30, no. 5, p. 19-20.
- Ingersoll, R. V., and Anonymous, 2001, Tectonostratigraphy of the Santa Monica Mountains, Southern California: AAPG Bulletin, v. 85, no. 6, p. 1126.
- Harvey, A. M., Wigand, P. E., and Wells, S. G., 1999, Response of alluvial fan systems to the late Pleistocene to Holocene climatic transition; contrasts between the margins of pluvial lakes Lahontan and Mojave, Nevada and California, USA: Catena (Giessen), v. 36, no. 4, p. 255-281.
- Jakes, M. C., 1980, Surface and subsurface geology of the Camarillo and Las Posas Hills area, Ventura County, California: Oregon State University, Corvallis, OR, United States (USA).
- Kamerling, M. J., and Luyendyk, B. P., 1979, Tectonic rotations of the Santa Monica Mountains region, western Transverse Ranges, California, suggested by paleomagnetic vectors: Geological Society of America Bulletin, v. 90, no. 4, p. I 331-I 337.
- Keller, E. A., Pinter, N., 2003, Active Tectonics; earthquakes, uplift, and landscape, 1st ed., 362 pp., Prentice Hall, Upper Saddle River, NJ.
- Kew, W. S. W., 1924, Geology and oil resources of a part of Los Angeles and Ventura counties, California, B 0753.
- Kile, M. B., McMillan, K., McNamara, J.E., Primas, T.M., Butler, G., 1991, Structural Geology of the westernmost Camarillo Hills, Ventura County, California, *in* Blake, T. F., ed., Engineering Geology along the Simi-Santa Roas fault sytem and adjacent areas, Simi Valley to Camarillo, Ventura, California.
- Kirby, M.E., Lund, S.P., and Bird, B.W., 2006, Mid-Wisconsin sediment record from Baldwin Lake reveals hemispheric climate dynamics (Southern CA, USA): Palaeogeography, Palaeoclimatology, Palaeoecology, v. 241, p. 267-283.
- Lajoie, K. R., Sarna-Wojcicki, A. M., Yerkes, R. F., and Cooper, J. D., 1982, Quaternary chronology and rates of crustal deformation in the Ventura area, California.
- Larsen, S. C., Agnew, D. C., and Hager, B. H., 1993, Strain Accumulation in the Santa-Barbara Channel - 1970-1988: Journal of Geophysical Research-Solid Earth, v. 98, no. B2, p. 2119-2133.
- Lopez, W. B., 1991, Depositional environments and provenance of the Saugus and San Pedro Formations, Las Posas and Camarillo Hills area, Ventura County, California, *in* Blake, T. F., ed., Engineering Geology along the Simi-Santa Roas fault sytem and adjacent areas, Simi Valley to Camarillo, Ventura, California.
- Luyendyk, B. P., Kamerling, M. J., and Terres, R., 1980, Geometric model for Neogene crustal rotations in southern California: Geological Society of America Bulletin, v. 91, no. 4, p. I 211-I 217.
- Mackin, J. H., 1948, Concept of the graded river: Geological Society of America Bulletin, v. 5, p. 463-511.
- McClay, K. R., and Buchanan, P. G., 1992, Thrust faults in inverted extensional basins, Chapman & Hall, London, United Kingdom (GBR).
- McNamara, J. E., McMillan, K., Lopez, W.B., Kile, M.B., Butler, G., Van Alstine, D., 1991, Saugus Formation stratigraphy, Camarillo Hills, Ventura County, California, *in* Blake, T. F., ed., Engineering Geology along the Simi-Santa Roas fault sytem and adjacent areas, Simi Valley to Camarillo, Ventura, California.

- Melton, M. A., 1965, The geomorphic and paleoclimatic significance of alluvial deposits in southern Arizona: *Journal of Geology*, v. 73, no. 1, p. 1-38.
- Meigs, A., Brozovic, N., and Johnson, M. L., 1999, Steady, balanced rates of uplift and erosion of the Santa Monica Mountains, California: *Basin Research*, v. 11, no. 1, p. 59-73.
- Mix, A. C., Bard, E., and Schneider, R., 2001, Environmental processes of the ice age; land, oceans, glaciers (EPILOG): *Quaternary Science Reviews*, v. 20, no. 4, p. 627-657.
- Nicholson, C., Sorlien, C. C., Atwater, T., Crowell, J. C., and Luyendyk, B. P., 1994, Microplate capture, rotation of the western Transverse Ranges, and initiation of the San Andreas transform as a low-angle fault system: *Geology (Boulder)*, v. 22, no. 6, p. 491-495.
- Onderdonk, N. W., Minor, S. A., and Kellogg, K. S., 2005, Taking apart the Big Pine Fault; redefining a major structural feature in Southern California: *Tectonics*, v. 24, no. 6, p. 11.
- Oskin, M., Sieh, K., Rockwell, T., Miller, G., Gupta, P., Curtis, M., McArdle, S., and Elliot, P., 2000, Active parasitic folds on the Elysian Park anticline: Implications for seismic hazard in central Los Angeles, California: *Geological Society of America Bulletin*, v. 112, no. 5, p. 693-707.
- Ponti, D. J., 1985, The Quaternary alluvial sequence of the Antelope Valley, California: *Special Paper - Geological Society of America*, v. 203, p. 79-96.
- Kirby, M. E., Lund, S. P., and Bird, B. W., 2006, Mid-Wisconsin sediment record from Baldwin Lake reveals hemispheric climate dynamics (Southern CA, USA): *Palaeogeography, Palaeoclimatology, Palaeoecology*, v. 241, no. 2, p. 267-283.
- Pazzaglia, F. J., Gardner, T. W., and Merritts, D. J., 1998, Bedrock fluvial incision and longitudinal profile development over geologic time scales determined by fluvial terraces: *Geophysical Monograph*, v. 107, p. 207-235.
- Quade, J., Forester, R. M., and Whelan, J. F., 2003, Late Quaternary paleohydrologic and paleotemperature change in southern Nevada: *Special Paper - Geological Society of America*, v. 368, p. 165-188.
- Ritter, D. F., 1967, Terrace development along the front of the Beartooth Mountains, southern Montana: *Geological Society of America Bulletin*, v. 78, no. 4, p. 467-483.
- Ruff, R., Shlemaon, R.J., 1991, Character and recency of faulting along a portion of the northern Springville fault, Camarillo, Ventura County, California *in* Blake, T. F., ed., *Engineering Geology along the Simi-Santa Roas fault sytem and adjacent areas, Simi Valley to Camarillo, Ventura, California*, p. 147.
- Shaw, J. H., and Suppe, J., 1996, Earthquake hazards of active blind-thrust faults under the central Los Angeles Basin, California: *Journal of Geophysical Research, B, Solid Earth and Planets*, v. 101, no. 4, p. 8623-8642.
- Sorlien, C. C., Kamerling, M. J., Seeber, L., and Broderick, K. G., 2006, Restraining segments and reactivation of the Santa Monica-Dume-Malibu Coast fault system, offshore Los Angeles, California: *Journal of Geophysical Research-Solid Earth*, v. 111, no. B11, p. -.
- Strahler, A. N., 1952, Hypsometric (area-altitude curve) analysis of erosional topography: *Geological Society of America Bulletin*, v. 63, no. 11, p. 1117-1141.
- Tierra Tech Testing Laboratory, 1978, Geologic reports for Tract 2910 and Tract 2930, eastern Camarillo (unpublished report).
- Treiman, J. A., 1997, Springville, Camarillo and related faults in the Camarillo and Santa Paula Quadrangles, Ventura County, California, Division of Mines and Geology, Fault Evaluation Report FER-237 (unpublished).

- Treiman, J. A., 1998, Simi-Santa Rosa fault zone in the Moorpark, Newbury Park, Simi Valley East, Simi Valley west, Thousand Oaks quadrangles, Ventura County, California, Division of Mines and Geology, Fault Evaluation Report FER-244 (unpublished).
- U.S. Geological Survey and Southern California Earthquake Scientists (USGS and SCEC), 1994, The magnitude 6.7 Northridge California, earthquake of 17 January 1994: *Science*, vol. 266, p. 389-397.
- Walls, C., Rockwell, T., Mueller, K., Bock, Y., Williams, S., Pfanner, J., Dolan, J., and Fang, P., 1998, Escape tectonics in the Los Angeles metropolitan region and implications for seismic risk: *Nature*, v. 394, no. 6691, p. 356-360.
- Wagner, H. M. L., E.B.; Roeder, M.A.; Prothero, D.R.; and McDaniel, G. E. J., 2007, A new Irvingtonian land mammal assemblage from the Saugus Formation, Moorpark, Ventura County, California: *Bulletin - Southern California Academy of Sciences*, v. 106, no. 2, p. 141.
- Weigand, P. W., Savage, K. L., and Nicholson, C., 2002, The Conejo Volcanics and other Miocene volcanic suites in southwestern California: *Special Paper - Geological Society of America*, v. 365, p. 187-204.
- Wells, S. G., Brown, W. J., Enzel, Y., Anderson, R. Y., and McFadden, L. D., 2003, Late Quaternary geology and paleohydrology of pluvial Lake Mojave, Southern California: *Special Paper - Geological Society of America*, v. 368, p. 79-114.
- Whitney, R. A., Gath, E.M., 1991, Structure, tectonics, and surface rupture hazard at the Las Posas anticline, Ventura County, California, *in* Blake, T. F., ed., *Engineering Geology along the Simi-Santa Rosa fault system and adjacent areas, Simi Valley to Camarillo, Ventura, California*, p. 164.
- Wright, T. L., 1991, Structural geology and tectonic evolution of the Los Angeles basin, California, *in* Biddle, K.T., ed., *Active margins basins: American Association of Petroleum Geologist Memoir 52*, p. 35-135.
- Yeats, R. S., 1988, Late Quaternary Slip Rate on the Oak Ridge Fault, Transverse-Ranges, California - Implications for Seismic Risk: *Journal of Geophysical Research-Solid Earth and Planets*, v. 93, no. B10, p. 12137-12149.
- Yeats, R. S., Huftile, G. J., and Stitt, L. T., 1994, Late Cenozoic Tectonics of the East Ventura Basin, Transverse Ranges, California: *Aapg Bulletin-American Association of Petroleum Geologists*, v. 78, no. 7, p. 1040-1074.
- Yerkes, R. F., Sarna-Wojcicki, A. M., and Lajoie, K. R., 1987, *Geology and Quaternary deformation of the Ventura area, scale 1:24,000*.

## **Appendix**



## **Santa Barbara Project**

Sixteen (16) sediment samples from California were taken for dating by optical stimulated luminescence (OSL). Except for three samples (Duane17, Duane18, Duane19), the samples were taken in March 2007 by Prof. Lewis Owen and Dr. Markus Fuchs (Department of Geology, University of Cincinnati, Ohio). Sample preparation and luminescence measurements were carried out at the Cincinnati Luminescence Laboratory, University of Cincinnati. Luminescence measurements and data analyzes were carried out by Dr. Markus Fuchs.

### **Background**

Optically stimulated luminescence (OSL) dating determines the time that has elapsed since sediment was last exposed to daylight (Aitken, 1998). The technique relies on the interaction of ionizing radiation with electrons within semi-conducting minerals resulting in the accumulation of charge in metastable location within minerals. Illuminating the minerals (typically quartz or K-feldspar) detraps the charge that combines at luminescence centers. This results in the emission of photons (luminescence). Prior to deposition, if the mineral is exposed to sufficient light all the trapped charge is detrapped and the sample are said to be bleached. Insufficient exposure to light results in partial bleaching and an over estimate of age. Artificially dosing sub-samples and comparing the luminescence emitted with the natural luminescence can determine the relationship between radiation flux and luminescence. The equivalent dose ( $D_e$ ) experienced by the grains during burial therefore can be determined. The other quantity needed to calculate the age is the ionizing radiation dose rate (DR). This can be derived from direct measurements or measured concentrations of radioisotopes.

The age is then derived using the equation:

$$\text{Age} = \frac{D_e}{DR}$$

The uncertainty in the age is influenced by the systematic and random errors in the  $D_e$  values and the possible temporal changes in the radiation flux, and the nature of the bleaching (reflecting the environment of deposition). The quoted error is the deviation of the  $D_e$  values on multiple sub-samples and the error in measured ionizing radiation dose rate or the concentration of radioisotopes. It is not possible to determine temporal changes in the dose rate that is a consequence of changes in water content and the growth and/or translocation of minerals within the sediment. The dose rate is therefore generally assumed to have remained constant over time. OSL ages on sediments have been determined for sediments ranging from a few decades to hundreds of thousands of year old. The precision of the dating is typically 5 to 20% of the age.

### **OSL dating procedure**

For OSL dating the quartz coarse grain fraction of 90-125  $\mu\text{m}$  was extracted from the sediments, using standard sample preparation techniques. Equivalent doses ( $D_e$ ) were determined using a standard single aliquot regeneration (SAR) protocol after Murray & Wintle (2000). All OSL measurements were carried out on a Risø-Reader TL/OSL-DA-15, equipped with blue LEDs ( $470 \pm 30 \text{ nm}$ ) for stimulation and a Thorn-EMI 9235 photomultiplier combined with a 7.5 mm U-340 Hoya filter (290-370 nm) for detection. Radionuclide concentrations for dose rate (DR) calculations were achieved by neutron activation analysis (NAA), measured at the USGS Nuclear Reactor Facility in Denver.

### **Results**

Radionuclide concentrations for dose rate (DR) calculations are based on NAA analysis of the sediments. The results for  $^{238}\text{U}$ ,  $^{232}\text{Th}$  and  $^{40}\text{K}$  concentrations and the resulting dose rates are given in Table 1.

Up to 48 aliquots (in average 24) were measured for  $D_e$  estimation. Bleaching tests showed after 2 h of daylight exposure a reduction of the luminescence signal to background level of the PM-tube. Dose recovery tests indicated the reproducibility of a given dose within  $1\sigma$  errors, using SAR with a preheat of  $220^\circ\text{C}$ . Estimated  $D_e$  values are given in Table 2.

### **Conclusion**

All samples show a high  $D_e$ -scatter with a high percentage of measured aliquots already in saturation. The high  $D_e$  scatter can be explained by insufficient bleaching of the quartz grains during the last process of sediment reworking. A precise determination of the  $D_e$  from the quartz extracts was therefore not possible. However, assuming insufficient bleaching of the quartz grains during their last sediment reworking, the lower part of the dose distribution might represent the best bleached grains. Therefore, a mean  $D_e$  was estimated from the lower part of the dose distribution. Age estimates are given in Tale 2.

**Tab. 1:Dose-rate Parameter.**

Sample depth, radionuclides, water content, cosmic and total dose-rate.

| Sample          | Depth<br>[m] | <sup>238</sup> U <sup>a</sup><br>[ppm] | <sup>232</sup> Th <sup>a</sup><br>[ppm] | <sup>40</sup> K <sup>a</sup><br>[%] | W <sup>b</sup><br>Δ | DR <sub>Cosm</sub> <sup>c</sup><br>[Gy a <sup>-1</sup> ] | DR <sup>d</sup><br>[Gy a <sup>-1</sup> ] |
|-----------------|--------------|--|---|-------------------------------------|---------------------|--|--|
| <i>Duane 1</i>  | 5            | 1.40±0.03                              | 4.27±0.03                               | 2.99±0.17                           | 1.15±0.07           | 0.15±0.01  | 3.25±0.25                                |
| <i>Duane 2</i>  | 5            | 1.48±0.03                              | 5.91±0.05                               | 2.77±0.18                           | 1.15±0.07           | 0.15±0.01  | 3.17±0.25                                |
| <i>Duane 3</i>  | 3            | 1.41±0.03                              | 4.29±0.03                               | 2.63±0.17                           | 1.15±0.07           | 0.17±0.01  | 2.96±0.23                                |
| <i>Duane 4</i>  | 6            | 2.06±0.04                              | 6.61±0.05                               | 2.81±0.19                           | 1.15±0.07           | 0.14±0.01  | 3.36±0.26                                |
| <i>Duane 5</i>  | 6            | 2.10±0.04                              | 7.96±0.06                               | 2.43±0.18                           | 1.15±0.07           | 0.14±0.01  | 3.12±0.25                                |
| <i>Duane 6</i>  | 6            | 2.13±0.04                              | 9.39±0.08                               | 2.34±0.19                           | 1.15±0.07           | 0.14±0.01  | 3.14±0.25                                |
| <i>Duane 7</i>  | 6            | 2.18±0.04                              | 9.41±0.07                               | 2.10±0.18                           | 1.15±0.07           | 0.14±0.01  | 2.95±0.24                                |
| <i>Duane 8</i>  | 9            | 2.21±0.04                              | 8.77±0.07                               | 2.22±0.19                           | 1.15±0.07           | 0.11±0.01  | 2.99±0.24                                |
| <i>Duane 9</i>  | 6            | 1.59±0.04                              | 5.14±0.04                               | 2.45±0.21                           | 1.15±0.07           | 0.14±0.01  | 2.87±0.24                                |
| <i>Duane 10</i> | 6            | 1.49±0.03                              | 4.89±0.04                               | 2.60±0.23                           | 1.15±0.07           | 0.14±0.01  | 2.96±0.26                                |
| <i>Duane 11</i> | 2            | 1.25±0.03                              | 5.59±0.05                               | 2.21±0.18                           | 1.15±0.07           | 0.18±0.01  | 2.66±0.22                                |
| <i>Duane 12</i> | 1            | 1.33±0.03                              | 4.13±0.03                               | 2.56±0.19                           | 1.15±0.07           | 0.20±0.01  | 2.90±0.23                                |
| <i>Duane 13</i> | 3            | 2.71±0.05                              | 7.93±0.05                               | 2.39±0.16                           | 1.15±0.07           | 0.17±0.01  | 3.25±0.25                                |
| <i>Duane 17</i> | 5            | 3.15±0.06                              | 11.80±0.09                              | 2.04±0.17                           | 1.15±0.07           | 0.15±0.01  | 3.25±0.25                                |
| <i>Duane 18</i> | 5            | 1.46±0.03                              | 6.04±0.05                               | 2.86±0.17                           | 1.15±0.07           | 0.15±0.01  | 3.26±0.25                                |
| <i>Duane 19</i> | 3            | 3.89±0.07                              | 12.40±0.10                              | 2.25±0.20                           | 1.15±0.07           | 0.17±0.01  | 3.64±0.28                                |

<sup>a</sup>Elemental concentrations from NAA of whole sediment measured at USGS Nuclear Reactor in Denver.<sup>b</sup>Estimated water content given in the Δ-notation (weight wet sample / weight dry sample).<sup>c</sup>Estimated cosmic dose-rate calculated after Barbouti & Rastin (1983) und Prescott & Stephan (1982).<sup>d</sup>Total dose-rate from beta, gamma and cosmic rays. Beta attenuation factors for <sup>238</sup>U, <sup>232</sup>Th and <sup>40</sup>K compositions incorporating grain size factors from Mejdahl (1979). Factors utilized to convert elemental concentrations to beta and gamma dose-rates from Adamiec and Aitken (1998) and beta and gamma components attenuated for moisture content.

**Tab. 2: Equivalent dose and OSL age estimates.**

Total dose-rate, aliquots, equivalent dose and OSL age.

| <b>Sample</b>                | <b>DR</b><br>[Gy a <sup>-1</sup> ] | <b>Aliquots<sup>a</sup></b> | <b>De<sup>b</sup></b><br>[Gy] | <b>Age</b><br>[ka] |
|------------------------------|------------------------------------|-----------------------------|-------------------------------|--------------------|
| <i>Duane 1</i>               | 3.25±0.25                          | 3                           | 65.26±7.95                    | 20.11±2.90         |
| <i>Duane 2</i>               | 3.17±0.25                          | 9                           | 81.94±11.38                   | 25.83±4.12         |
| <i>Duane 3</i>               | 2.96±0.23                          | 4                           | 95.59±17.07                   | 32.27±6.29         |
| <i>Duane 4</i>               | 3.36±0.26                          | 14                          | 93.32±2.13                    | 27.79±2.28         |
| <i>Duane 5</i>               | 3.12±0.25                          | 3                           | 91.04±19.71                   | 29.15±6.71         |
| <i>Duane 6</i>               | 3.14±0.25                          | 7                           | 93.32±4.73                    | 29.73±2.83         |
| <i>Duane 7</i>               | 2.95±0.24                          | 25                          | 120.06±5.96                   | 40.76±3.81         |
| <i>Duane 8</i>               | 2.99±0.24                          | 16                          | 54.62±2.85                    | 18.26±1.76         |
| <i>Duane 9</i>               | 2.87±0.24                          | 4                           | 98.55±27.31                   | 34.39±9.96         |
| <sup>c</sup> <i>Duane 10</i> | 2.96±0.26                          |                             | Min. 136.56                   | Min. 46.17         |
| <i>Duane 11</i>              | 2.66±0.22                          | 14                          | 50.41±5.29                    | 18.94±2.52         |
| <i>Duane 12</i>              | 2.90±0.23                          | 6                           | 78.18±9.99                    | 26.92±4.06         |
| <i>Duane 13</i>              | 3.25±0.25                          | 6                           | 80.23±2.09                    | 24.69±1.98         |
| <i>Duane 17</i>              | 3.25±0.25                          | 19                          | 40.97±3.21                    | 12.60±1.38         |
| <i>Duane 18</i>              | 3.26±0.25                          | 8                           | 62.70±3.74                    | 19.24±1.88         |
| <i>Duane 19</i>              | 3.64±0.28                          | 21                          | 17.41±1.07                    | 4.78±0.47          |

<sup>a</sup>Number of used aliquots for De determination.<sup>b</sup>Errors are 1-sigma standard errors<sup>c</sup>sample was in saturation, thus only a minimum age could be calculated